CONDITION MONITORING OF A WING STRUCTURE FOR AN UNMANNED AERIAL VEHICLE (UAV)

by

THUBALAKHE PATRICK MASANGO

Thesis/Dissertation submitted in fulfilment of the requirements for the degree

Master of Technology: Mechanical Engineering

in the Faculty of Engineering

at the Cape Peninsula University of Technology

Supervisor: A/Prof Dr Oscar Philander
Co-supervisor: Mr Mornay Riddles

Bellville

September 2015

Declaration

I, Thubalakhe Patrick Masango, declare that the contents of this dissertation/thesis represent my own unaided work, and that the dissertation/thesis has not previously been submitted for academic examination towards any qualification. Furthermore, it represents my own opinions and not necessarily those of the Cape Peninsula University of Technology.

Signed	**Date**

Abstract

Currently non-destructive testing techniques for composite aircraft structures are disadvantaged when compared to online Structural Health Monitoring (SHM) systems that monitor the structure while in-service and give real time data. The present research work looks at developing a protocol for online structural health monitoring of a UAV wing structure using PVDF film sensors, especially including the monitoring of structural changes caused by defects. Different types of SHM techniques were studied in relation to carbon fibre composites. Laminate composite make-up and manufacturing process was investigated and vacuum infusion process was used to manufacture the samples that resemble the Guardian II wing structure, then the three-point bending test was used to determine the material properties. Digital Shearography was employed as a stationery non-destructive technique to determine the sensor to structure attachment, type and position of defects that affect the state of performance. Finite Element Analysis (FEA) was done using ANSYS Workbench which served as a modelling tool using a drawing imported from Solid-works. Experimental investigation was done using PVDF sensor embedded on the surface of the sample in a cantilever setup and a vertical Vernier scale to measure the deflection due to impact and vibration loading. A Fluke-View oscilloscope was used as a data logger when the measurement of the output voltage and the natural frequency were recorded. The techniques of using FEA and experimental investigation were then compared. The findings of this study showed that the PVDF sensor is suitable for condition monitoring of a UAV wing structure.

Key words

Polyvinylidine fluoride (PVDF), Digital Shearography, Structural Health Monitoring (SHM).

Acknowledgements

This project was made possible by a number of people, and their contribution is highly appreciated. I want to acknowledge my supervisor Prof Philander for being a mentor, a brother and leading by example and also the support I got from Mr. Riddles as co-supervisor. Thank you to Prof Gryzagiridis for his guidance and for continually evaluating my work. My family for their love and support on my studies on which without them the completion of this project would never have been possible. Also I give thanks to my kids and their mother (Ncobile) for their love and support. I also want to thank Vuyani Moni for helping with the three-point bending test and Nceba Dwane for helping with the Digital Shearography test. I am truly greateful for the support I got from Mr Kohlhofer for his assistance in the testing equipment and the advice through the project and thank the Lord almighty for leading my life until this point.

Table of Contents

List of figures

List of tables

Glossary

PVDF	Polyvinilydine Flouride
UAV	Unmanned Aerial Vehicle
SHM	Structural Health Monitoring
AMTL	Advanced Manufacturing Technology Laboratory
UCT	University of Cape town
CPUT	Cape Peninsula University of Technology
FEA	Finite Element Analysis
NDT	Non-Destructive Testing
FEA	Finite Element Analysis
FFT	Fast Fourier Transform
PZT	Lead Zinconate Titinate
CCD	Charge Couple Device

Nomenclature

Symbols and letters

Y - Young's Modulus

I - Second Moment of Area

l - Length

b - Breadth

ρ - Density

$\dfrac{dy}{dx}$ - Slope

y - Displacement

ε - Strain

C - Capacitance

h - Thickness

Chapter one

1. Introduction and background study

1.1   Problem Statement

The Department of Mechanical Engineering of the Cape Peninsula University of Technology established a Drone or Unmanned Aerial Vehicle (UAV) development programme in 2008. The primary objective of the programme was to develop fixed and rotary wing technology demonstrator platforms to test and mature Morphing and Structural Health Monitoring technologies for the aeronautical industries. This study looks at developing the latter technology to ensure reduced down time maintenance of the laminate composite sub-structure of one of these platforms, the Guardian II, Unmanned Aerial Vehicle.

The majority of load bearing structural components used in different areas of engineering require periodic inspections of their integrity and assessment of accumulated in-service damage as part of their safety and maintenance requirements. Both costly in monetary terms and down time, these operations can be replaced by a new genre of inspection techniques called online structural health monitoring. This new technology requires the placement of sensors in the structure permanently that can be interrogated continuously or periodically or as the need arises. There are emerging local and international markets for composite structural health monitoring systems for them. The currently used damage detection methods in the aeronautic industry include visual as well as localized Non Destructive Testing (NDT) techniques such as Ultrasonic inspection, Acoustic emission, Radiography, Eddy-current, laser ultrasonic, vibration analysis and lamb

waves [1]. The need for quantitative global damage detection methods that can be applied to a complex structure such as an Unmanned Aerial Vehicle (UAV) has led to the development and continued research of methods that can examine adverse changes in the performance of the composite structure while in-service and provide real-time data. Online structural health monitoring using Polyvinilydene Fluoride (PVDF) sensors and the development of a protocol for parameter sampling for a UAV wing structure would be of interest to the aeronautic industry. Structural health monitoring of smart composite material by acoustic emission was investigated using the ceramic piezoelectric sensor known as PZT (Lead Zinconate Titinate) [2]. This study however looks at the feasibility of using a polymeric piezoelectric sensor because it is flexible as compared to PZT, which is brittle.

1.2   Objectives

In order to achieve a workable Online Structural Health Monitoring system for use in the composites industry, critical objectives must be achieved. These include:

1.2.1   Identifying the type, make-up and material properties of the composite to be used.

1.2.2   A method for determining online damage identification, this requires the identification of a particular sensor for the work environment.

1.2.3   Determining the geometric location of a particular flaw, using the identified sensors to develop a location algorithm to determine where the flaw is located in the overall structure

1.2.4   Quantification of the severity of the flaw, using material properties, fracture mechanisms, and damage mechanisms to determine the severity of the particular flaw

1.2.5 Predicting the available and\or remaining life of the overall structure with the included flaw.

1.3 Methodology

This study finds its origins in the Unmanned Aerial Vehicle (UAV) Development programme located in the Department of Mechanical Engineering of the Cape Peninsula University of Technology. The first of these vehicles were developed by staff and students of the Department in and around 2008. To this end, the laminate composite composition and its manufacturing processes have been established. In order to achieve the first objective, a presentation on the laminate composite and its manufacturing processes will be presented.

A review of sensors will be conducted to determine the particular sensor to be used in this Structural Health Monitoring study. Both healthy i.e. laminate composite specimens with and without sensors; and unhealthy/flawed samples will be manufactured and tested to determine their material properties. Both three-point-bending and cantilever mechanical tests will be employed to determine the latter. These tests will also be used to determine a link between the flaw and its location to the sensor thus achieving the third objective.

The fourth and fifth objectives will be achieved through using theories of fracture and damage mechanics to determine life prediction of the overall specimens in a particular energised environment and overall conclusions and recommendations will be made to determine the suitability of the studied method to the overall Structural Health Monitoring of a UAV wing.

1.4 Related Literature

Composite materials are made up of two or more different material at a macroscopic level to form new properties that cannot be achieved by those individual components in isolation. They have reinforcing and matrix phases. When compared to traditional metallic materials, composites have the advantage because of low density, high strength and stiffness, long fatigue life and high wear, creep, temperature resistance and corrosion [3]. Due to that fact, the composite materials are widely used in the aeronautic structures. Composite structures have many advantages over other materials but they are not exempted from some disadvantages. Material properties are very much depended on the manufacturing process and mechanism of flaw initiation, so damage evolution and fracture behaviour remains a challenge especially in complex structures. There is a lack of composites data and standards for design purposes, the structural efficiency depends on the designer's expertise and experience and is susceptible to be over-designed [4].

Damages in composite structures usually occur beneath the top surfaces and are barely visible to a human eye and they degrade the performance of the structure and they are not detected earlier, they can lead to catastrophic structural failures. As explained earlier, the non-destructive testing methods require that the structure must be stationery and sometimes the structure must be disassembled to ensure inspection of complex structures that can be costly, time consuming and labour extensive [5].

A technology of combining advanced sensors with intelligent algorithms to continually interrogate structural health condition and provide real-time and on-line damage detection can be achieved in Structural Health Monitoring (SHM). This technique has potential benefits of improving safety, reliability, reducing lifecycle costs and assists in the design of composites

structures. Different sensors are integrated and attached to the host structure to monitor structural integrity such as stress, strain, temperature, etc. The popular sensors that are used in structural health monitoring and give online information are the following: strain gauges, fibre optic sensors, eddy current sensors, micro-electro-mechanical systems (MEMS) sensors and piezoelectric sensors [6]. SHM technology has advantages and disadvantages and the final choice of the sensor will always depend on a particular application.

The sensors themselves have a load bearing ability and SHM system is greatly simplified compared to other techniques. SHM methods can either be passive or active depending on whether the actuator is used. Passive SHM only listens to the structure and does not interact with it where else in active SHM, the structure is excited with and actuator and interrogated by the analysing the received responses. The common active SHM methods are lamb wave, electromechanical impedance and active vibration based methods (the one used in this study). The common passive SHM methods include acoustic emission, strain based method and Comparative Vacuum Monitoring (CVM) method. Active sensors are the ones which respond to strain by outputting a voltage proportional to the strain but capable of producing strain (force) when voltage is applied to them. Passive sensors are the ones that respond by changing their electrical resistance or optical characteristics or magnetic properties when strain is applied [7].

1.4.1 Strain gages

Strain gauge is a device that measures strain on a structure by changing its resistance; it is a force transducer that has a spring body that converts the mechanical stresses into strain that is picked

up by the strain gauge. The strain gauge produces a linear relationship between strain and change in resistance; that is governed by the following equation [8]:

$$\frac{\Delta R}{R} = k * \varepsilon$$

Where ΔR is the chance in resistance, R is the resistance of a strain gauge, k is the gauge factor of the strain gauge and ε is strain.

The other typical types of strain gauges include a foil strain gauge and a semiconductor strain gauge. These gauges are normally connected to a Wheatstone bridge. For a single active gauge, there must be three dummy resistors to complete the bridge. Strain gauges work on an excitation voltage with a typical value of 5 V – 12 V and a typical output in millivolts [9]. Because the output signal is very small, an additional circuit is needed to amplify the output signal. Different types of strain gauges are selected for certain application depending on the operating environment for example temperature, humidity, electromagnetic interference etc.

1.4.2 Fibre optic sensors

Fibre Optical Sensors (FOS) is one of the promising structural health monitoring sensor for intelligent monitoring systems that would enable continuous load monitoring and defect detection in composite aircraft structures while in-service. The normally used FOSs include inteferometric sensors such as Michelson, Mach-Zehnder and Fabry-Perot which can measure strains and deformation by detecting the phase shift of relative optical waves at local sites [10]. There are several types of SHM sensors available but the FOS particularly those that are based on Fibre Bragg Grating (FBG) are increasingly interesting technology because of their distinctive advantages including sensitivity, immunity to electromagnetic interference and durability.

Multiplexing capabilities of FOS have a possibility to reduce complicated wiring such as the one for strain gauges and besides that FBG based measurements systems there are other techniques based on Rayleigh or Brillouin scattering of light in standard telecom optic fibre where the whole fibre act as a sensor with a range in centimetre or lower.

There is a specific concern in defect detection sensor known as piezoelectric sensor which is considered to be the excellent candidate is likely to be in the developmental stage to have multiplexing capabilities, lower durability and inferior strain to failure resistance. However the wider acceptance of this sensing system remain a challenges regarding sensor performance especially when embedded, structure size and weight to sensor size and weight and the lack of standardisation and certification [11]. The major disadvantage of using fibre optic sensor are the following, the monitoring system may be complex and have a high cost, the requirement for precise installation procedures and to develop a user friendly measuring systems is complex [12].

1.4.3 Eddy current sensors

Eddy current sensors works on a principle of using eddy currents from electromagnetic induction to detect defects in metallic structures. These sensors detect mostly corrosion and cracks which makes it ideal for metal matrix composites. The challenge is on integrating the winding configuration which was overcame by micro-fabrication technique, where the windings were printed directly to a conformable substrate and can be attached on a surface or embedded to a structure making it possible for online SHM [13]. These sensors are susceptible to magnetic interference and can be difficult to integrate them to complex structures, so careful interpretation of the output signal is very important to distinguish between the relevant and non-relevant signals.

1.4.4 MEMS sensors

Micro-electro-mechanical-systems are the integration of mechanical sensors and actuators with electronics on a common silicon substrate by using micro-machining technology. MEMS are different from Integrated Circuits (IC's). MEMS are a combination of semiconductor processing and mechanical engineering at a very small scale. IC's can be taken as the brain of the system while MEMS augments the decision making capabilities with eyes and arms to allow the microsystem to sense and control the environment. MEMS can be classified into sensors and actuators. MEMS can be integrated onto a single silicon chip with the accelerometer and the needed electronics. These systems are some of the greater achievements in micro-machining, they consists of micro-sensors (inputs), circuits (processing) and micro-actuators (output). The power supply can also be compact to the same scale but till present it is still a challenge [14].

Research is continually conducted under these systems, according to Michael Roukes [15], the future for MEMS is NEMS (Nano-Electro-Mechanical-Systems) which can be built with masses of few Otto-grams (10^{-8} grams) with a cross-section of about 10 nanometres. Although there is an existing technology to create NEMS there are challenges in achieving a communication signal from nanoscale to macroscopic world, understanding and controlling mesoscopic world, quantum mechanics on the rate at which energy can be dissipated in small devices by vibrations and reproduction of these devices is complex and almost unachievable [15].

1.4.5 Piezoelectric sensors

Piezoelectric sensor is a transducer that is mostly used for sensing application; piezoelectric is a Greek word that means pressure to electric convection and conversely, it is amongst the fasted

growing technology because of the demand in the microprocessor industry. Piezoelectricity was discovered by the Curie brothers about hundred years ago and in the 1960's and intense research was conducted to see if there can be any material that can display piezoelectricity since it was discovered that a whale bone and tendon displayed some weak piezoelectric effect. It was only in 1969 when Kawai discovered a fluoro-polymer known as Polyvinylidine Fluoride (PVDF) which showed a very high piezo-activity when polarised [16]. See appendix A for PVDF sensor properties and its Copolymers.

PVDF behaves like ferroelectric materials; it produces electric charge if there is a change in mechanical strain or stress level and vice-versa but again it will also react to the change in external temperature by giving out an electric charge which is known as a pyro-electric effect. Because of its sensitivity to temperature change, it has an ability to absorb infrared energy that can amount to the heat from a human body at the region of 7 to 20µm wavelength spectrum.

It is worth mentioning that PVDF was not the only material that was discovered in the 19th century but there were others like nylon and PVC but PVDF was the one that exhibited stronger piezoelectric effect. PVDF film in its static mode will behave like a strain gauge with the exception that it does not require external power source to function as it produces more than 10 milli-volts (mV) per micro-strain (µε), about 60 dB higher than the voltage output of a foil strain gauge. PVDF film sensor has the properties similar to a capacitor, it has Silver ink coating on both side and the PVDF material is sandwiched between the metallization [16], see figure 1.
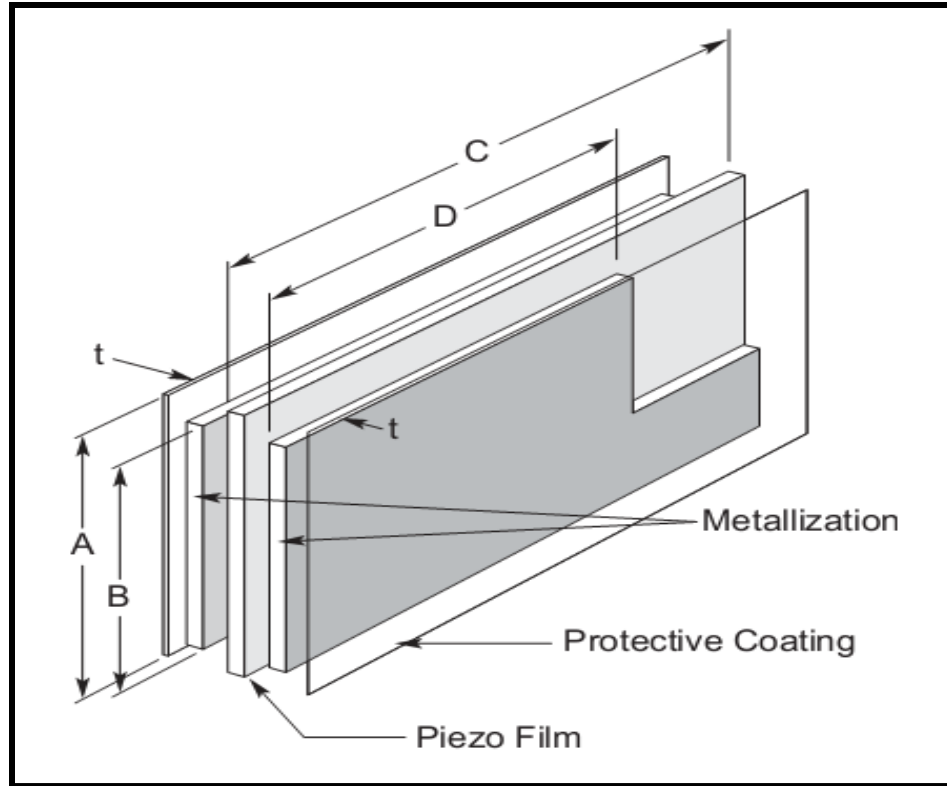
Figure 1.1: DT series piezoelectric film sensor [16]

PVDF film sensors are available in different sizes and thicknesses, like 28 µm and 52 µm respectively. For metallization there is the choice of silver ink as well as sputtered metallization however silver ink is preferable when attaching wire leads. The standard sputtered metallization is 700 Å of copper covered with 100 Å of nickel change Nickel-Copper (NiCu) alloy to Copper (Cu) with Nickel (Ni) provides good conductivity and is resistant to oxidation.

Polyvinylidene fluoride is a thin flexible polymer which has a low density and excellent sensitivity yet it is mechanically tough. PVDF film is well suited to strain sensing applications requiring very wide bandwidth and high sensitivity. The voltage generated by the sensor is collected by the conductive coating on both sides of the film. If the sensor output is proportional

to the changes in surface displacement, then the PVDF can be used to detect and monitor behaviour and stresses acting within a material. Like strain gauges the PVDF film needs to be firmly secured on the material under stress in order to translate the material's displacement into a strain in the PVDF film [17]. Piezoelectric sensors are used for measuring low or high frequency vibrations such as Lamb waves or acoustic emission and they are more desired for SHM because of their light weight, size and low cost. They can be employed as actuators and sensors especially Lead Zirconium Titenate (PZT) ceramic which has excellent sensitivity as a sensor and strong driving abilities as an actuator because of its high piezoelectric constant. PZT is a ceramic; it is brittle so it can easily break if attached to flexible structures. PVDF on the other hand is a polymer that is flexible with large compliance and poor inverse piezoelectric properties is used as a sensor [18].

1.4.6 Structural Health Monitoring methods for composite materials.

Common damages encountered in the UAV structure are leading edge erosion and related cracks, delamination and fibers failure or breakages due to low speed impacts, ballistic impact, fatigue and matrix cracks. The 2007 Ben Franklin Structural Health Monitoring Workshop discussed research on damage detection methods (caused by ballistic impact) [19]. See figures 1.1 and 1.2. A three-point bending test can be used to investigate the sensors response at failure and PVDF sensor has a capability to detect that. Since the currently used Non-Destructive-Techniques require that a structure be stationery or sometimes be dismantled/taken apart to scan for hidden defect then SHM using online monitoring methods are a viable solution to this challenge.

11

Figure 1.2: Ballistic impact [19]
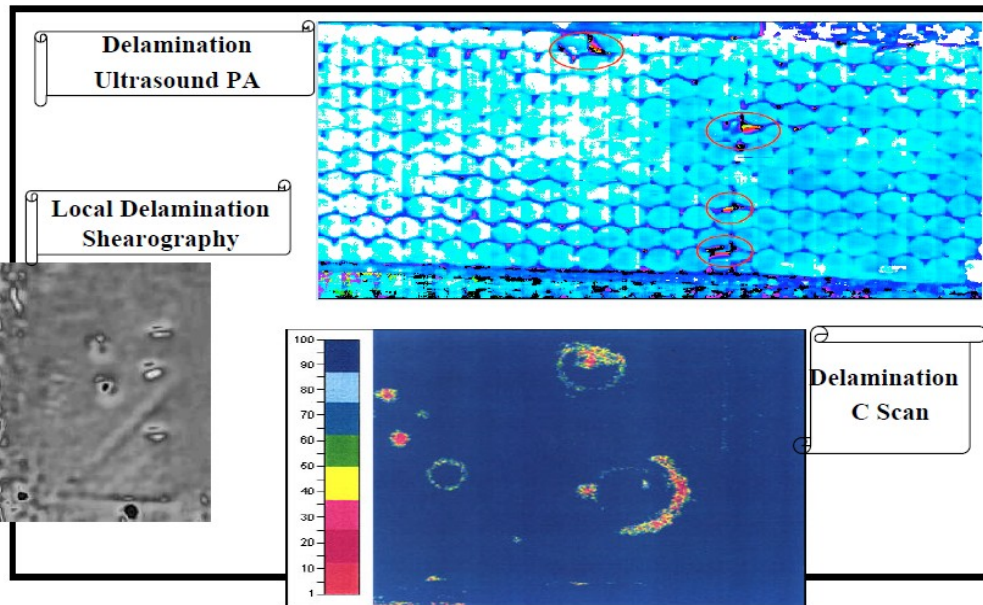
Figure 1.3: Skin-core delamination [19]

As mentioned earlier, SHM can be performed in either passive or active ways depending on whether the actuator is used on not. The typical passive approaches include Acoustic emission (AE), strain-based and the active approaches include Lamb waves, Electro-mechanical (E/M) impedance and active vibration-based method.

Acoustic emission is a sudden release of local strain energy due to change in structural integrity; this energy is released in a form of transient elastic wave. These waves originate from the AE source and captured by the sensor which is the converted to an electrical signal for interpretation to evaluate structural condition as mentioned in [2]. Strain-based method uses strain gauges and fibre optic sensors to measure strain distribution and is normally based on an array of multiplexed Fibre Bragg Grating.

Lamb waves are usually excited and received by PZT, PVDF and FOS have an ability as well due to multi-mode and dispersion characteristics but propagation of Lamb waves is very complicated. E/M impedance is based on a feedback mechanism, it is a ratio of applied force to the resulting velocity and that can be affected by defects however direct measurement of it is very hard. Active vibration-based method is the easiest one in SHM because it can either be model based or non-model based. It is recommended for complex and large structures because for un-practical measurements, Finite Element Analysis may be employed. It uses a vibration response to detect defects in a structure [20].

1.5   Scope and limitations of project

The Guardian II, Unmanned Aerial Vehicle wing structure is made up of carbon fibre layers that are bonded by epoxy and they are susceptible to damage caused by delamination, corrosion, ballistic impact etc. Although some research work has been done to explore these effects, it has been limited to non-destructive techniques that require a UAV to be stationery for scanning or use monitoring sensors that consume extra battery power to operate. There is a need for workable SHM technique that will give a real-time data while the structure is in service. Therefore the scope of this project was as follows:

- A case study using the proposed SHM technique for damage detection on a UAV wing structure.

- Manufacturing of the UAV wing structure samples and determining the material properties using three-point bending test. These material properties will be used in Finite Element Analysis (FEA) for simulating the samples in ANSYS Workbench software.

- The use of Digital Shearography to investigate sensor to structure attachment and explore the presence and severity of the damage in that structure.

- Conduct an experiment where the PVDF sensor will be attached on the UAV wing sample and tested on a cantilever mechanical test for the presence of flaws. The experiment and simulation results will be compared so as to draw a conclusion on the feasibility of using PVDF sensor for condition monitoring of a UAV wing.

- Determining the geometric location of a particular flaw, using PVDF to develop a location algorithm to determine where the flaw is located in the overall structure.

The limitations were as follows:

- The samples that were tested were limited to one degree of freedom.

- Fracture mechanics and damage mechanism to determine the severity of the particular flaw was not conducted in this study. This point addresses objective 1.2.4 which was partly achieved.

- Predicting the available and/or remaining life of the overall structure with the included flaw was also not conducted in this study. This is objective 1.2.5.

Chapter two

2   Laminate Composite Makeup and Manufacturing Process

2.1   Vacuum Resin Infusion Process

This process is used to manufacture the laminate composite sub-structure of the Guardian II UAV is the Vacuum Resin Infusion Process. It is a technique to produce a composite material using different layups of dry fibre laminates and epoxy or resin which is driven through the fibres by vacuum. It has been applied widely in the marine, automotive and aeronautic industries. The difficulty with the infusion process is that each size and shape of component requires a different layup design to allow a complete flow of resin without lock-off areas of dry laminate, or resin running too quickly through one section which may create voids. (See figures 2.1 and 2.2 for a schematic of the vacuum infusion composite moulding process)
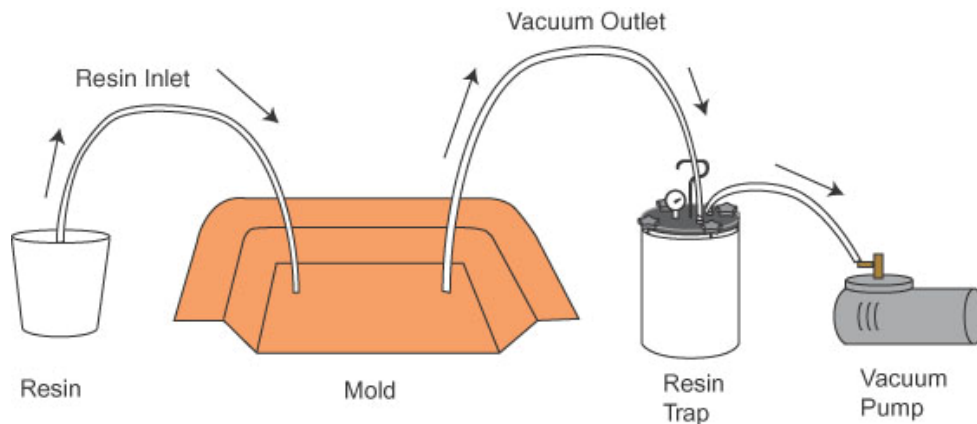
Figure 2.1: Vacuum infusion process [21]
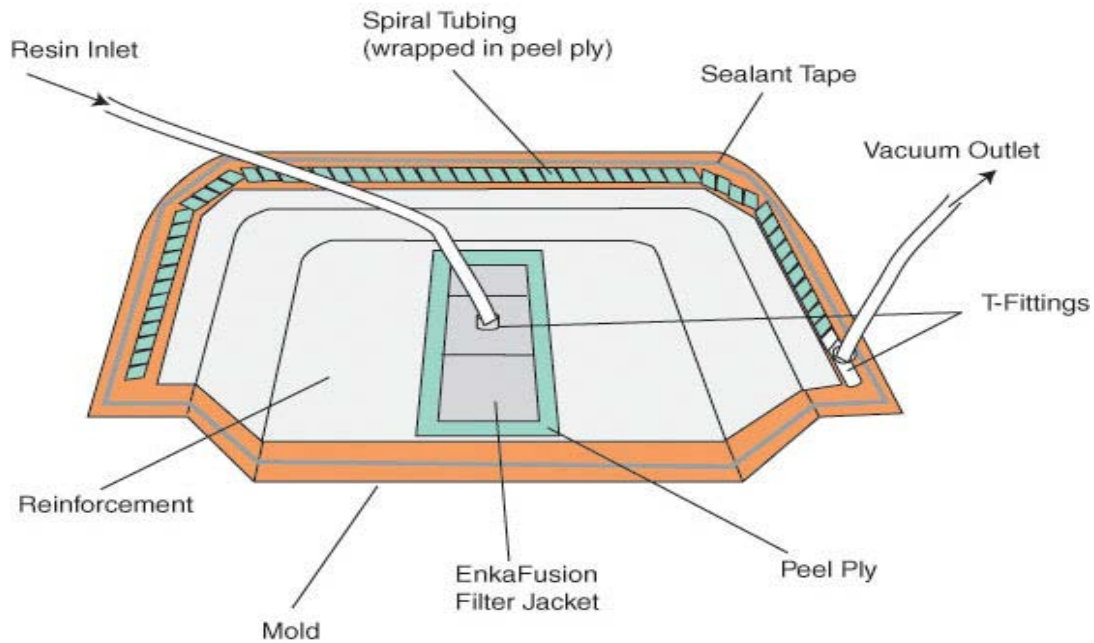
Figure 2.2: Vacuum infusion process layout [21]

2.2   Composite Laminate Sample Production

Due to advances in the Aerospace industry there is a rapid growth in the manufacturing of composite structures that can be lighter and manufactured at low cost, using high performance manufacturing techniques. This has lead the Aerospace industry towards the pre-impregnated materials where pressure and vacuum are used to form material plies into optimized mechanical property composites; central to this being vacuum infusion.

To ensure a smooth finish on the composite structure, the surface on which the material plies will be laid must be smooth and void free. In this case the voids are the gaps in the dry fibres and the resin is allowed to fill these whilst being drawn towards the vacuum source. In order to ensure the clean and smooth surface for the laminates used in this study, the glass table was cleaned four times with a Wax.

17

Figure 2.3: Waxing the glass table

The vacuum pump should be capable of 950 mbar and above but also to operate at a reduced vacuum level with a flow of air for more than 24 hours (as this process is based on slow curing abilities and at ambient temperatures). To ensure that there was no air passing through, a sealant tape was used and the vacuum pump was checked if it was still in order and the oil level was sufficient. The sealant tape was used to connect the reservoir and the vacuum chamber with a pipe. As seen in figure 3.2, this picture was taken before connecting the suction pipe from the lay-ups.

Figure 2.4: Vacuum chamber, pump and reservoir

The adhesive used consisted of Epoxy resin and Prime 20 LV, with a mixing ratio of 100:26. Epoxy resin was 100 g and Prime 20 LV was 26 g.
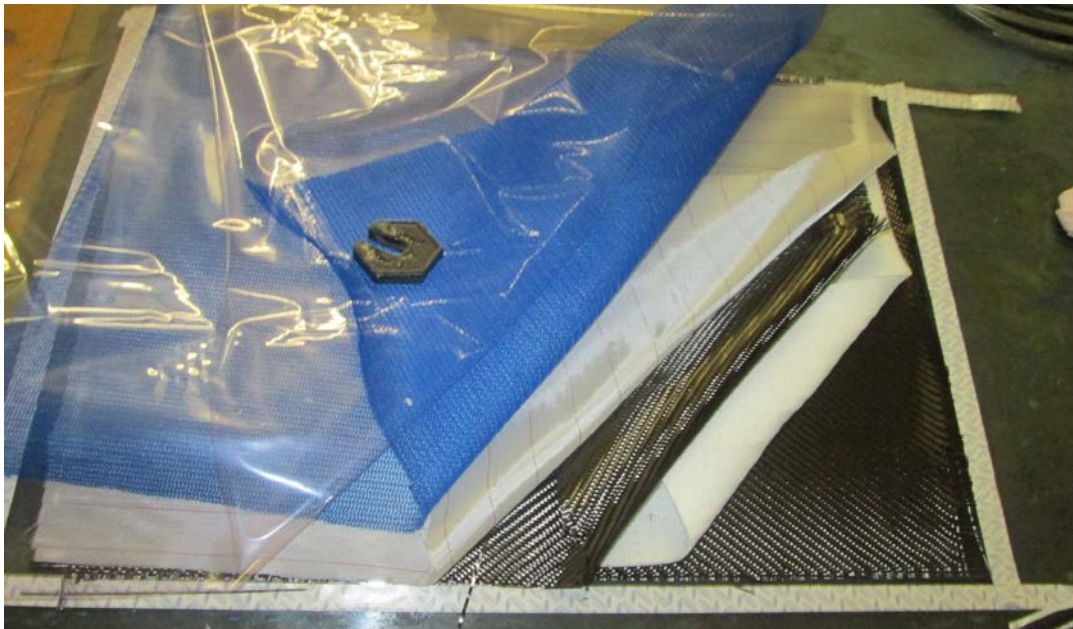
Figure 2.5: Layup of the laminates

Four lay-ups were manufactured at the premises of AMTL of sufficient size (90 cm X 80 cm) in order to cut enough specimens for testing. The lay-up was arranged in a bidirectional orientation as shown in figure 2.5 in the order of carbon fibres at the bottom, comet, carbon fibres, mesh and plastic. Mesh was used as a layer for pilling off the plastic, leaving two carbon fibre layers with comet sandwiched between them.

Figure 2.6: Putting the sealant tape

The sealant tape was used to cover the sample and the pump was switched on to suck out all the air in the sample. There were no leaks in the sample. The clamp that was put on the suction side was removed to let the resin to flow into the sample.
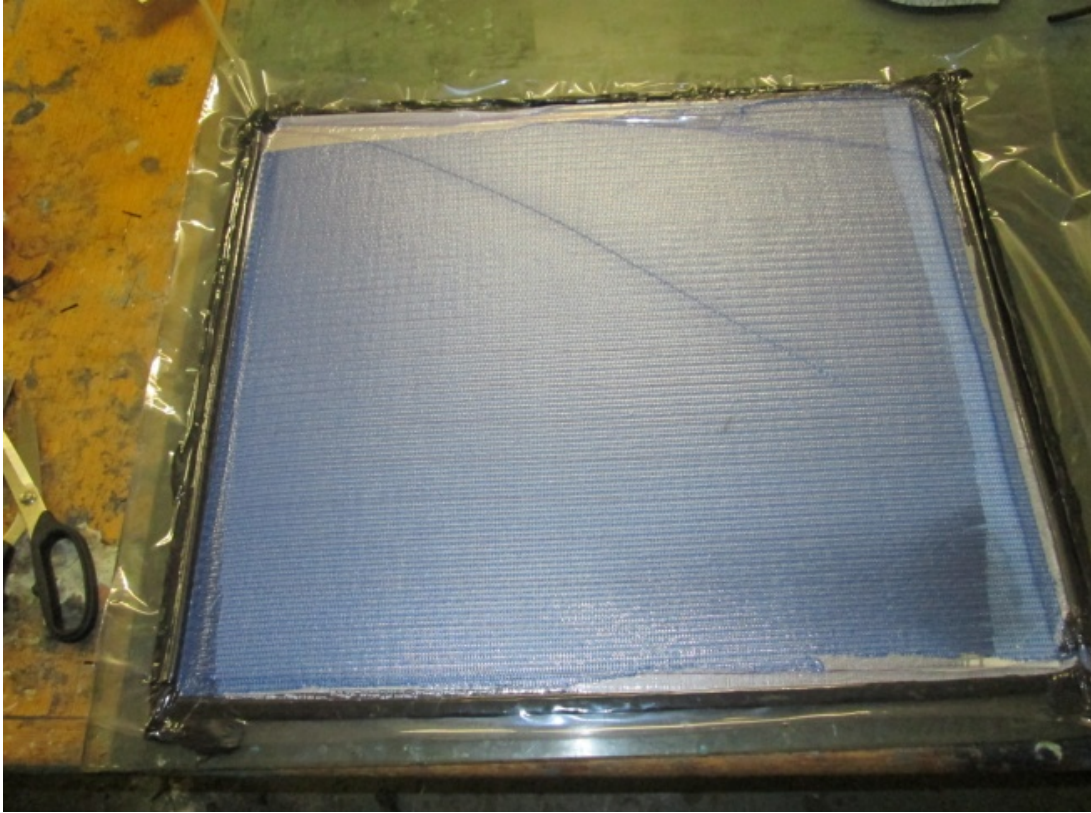
Figure 2.7: Creating vacuum in the sample

On the suction side a mixture of Epoxy resin and Prime 20 LV was put to flow freely in to the chamber. The samples were left in the laboratory for 24 hours at room temperature under vacuum for curing. The samples that were manufactured resemble that of the UAV wing which has a bidirectional structure. After curing, specimens of 280 mm X 69 mm X 2 mm were cut using a diamond saw. The cut samples were used to determine the material property that resembles that of Guardian II wing structure.

The material's properties were determined using a three-point bending test and numerical calculations were performed. The properties that were determined were the Young's Modulus (E), moment of inertia (I) and the maximum flexural strength (σ).
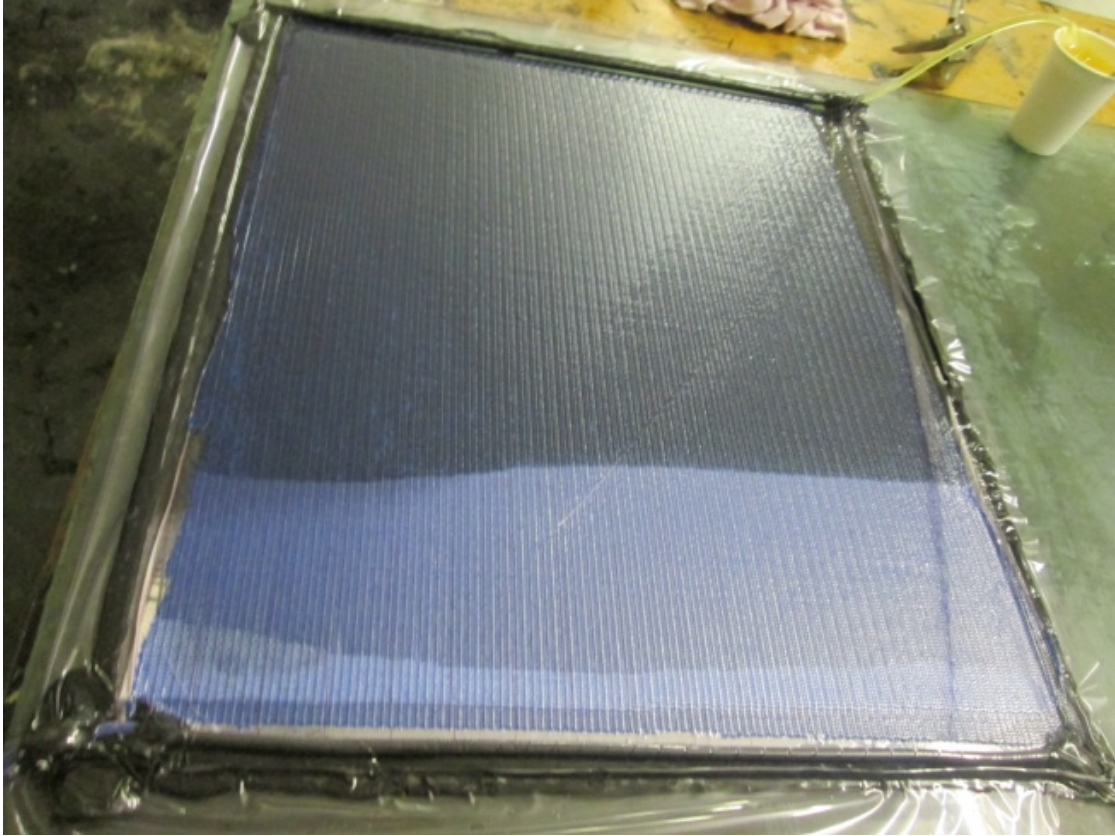
Figure 2.8: Flow of resin into the sample

Chapter three

3 Sample Testing and Methods used in this study

3.1 Three-Point Bending Test

The advantage of using three-point bending is the ease of preparing the specimen but the results are sensitive to the loading geometry and strain rate. This test also investigates the integrity of PVDF film sensor attachment to the structure so as to choose the best sensor attachment method and the epoxy to be used for embedding the sensor within the structure. The following diagram is an illustration of a three-point bending test showing the maximum bending moment at the loading position.
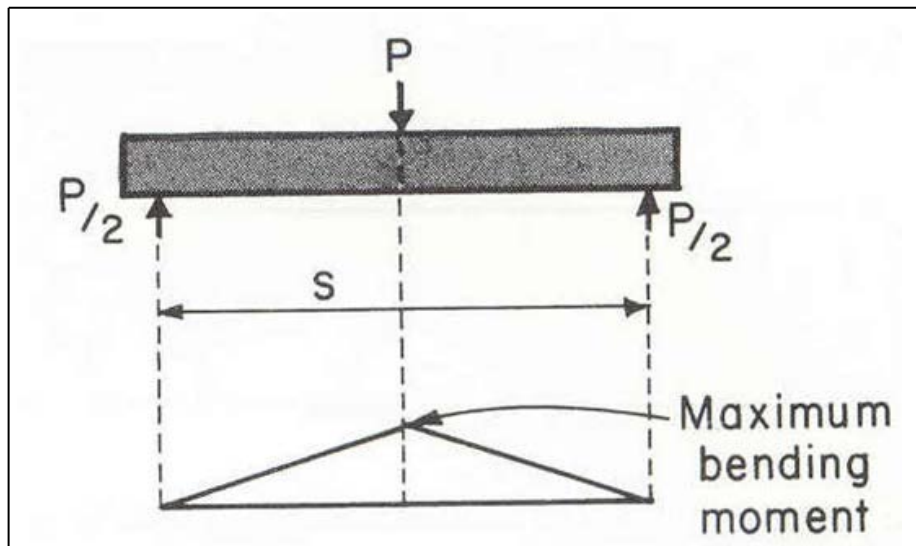
Figure 3.1: Three-point bending [22]

The results obtained from the three-point bending experiment are interpreted using the following equations:

$$\sigma = \frac{My}{I} \qquad\qquad \text{Equation 3.1}$$

$$\delta = \frac{PL^3}{48EI} \qquad\qquad \text{Equation 3.2}$$

Where M = P· S/2 is the moment applied at the middle of the composite specimen, y is the distance from the centre or neutral axis of the specimen to the surface, I is the moment of inertia of the beam depending on its cross sectional area, σ is the maximum flexural stress of the specimen, E is the Young's modulus of the material, P is the load exerted on the specimen shown at the mid-point of the beam in figure 3.1, S is the distance between the two supports where the specimen is placed and δ is the maximum deformation on the specimen.

3.1.1 Determining the material properties using three-point bending test

There were four samples that were cut using a diamond saw mounted on the workbench. The sizes of the samples were measured to be the same and introduced to a three-point bending test. The dimensions of each beam were as follows: 280 mm in length (l), 69 mm in breath (b) and 2 mm in thickness (h) because of the three-point bending standard where the ratio of length to breath must be 4:1. The Jig that was used was designed in the laboratory according to the standards, with the dimensions of 200 mm (L) between the supports, 0.3 mm on each side after the supports and 80 mm width on the inside where the specimen sits. The loading of the beam was arranged to be exactly in the middle (at L/2) as seen on figure 3.2. The beam was placed between the supports with the clearance of 40 mm on each side after the supports. That was done to keep the sample supported even after it had failed.

Figure 3.2: Specimen in a three-point bending jig

Figure 3.3: Specimen in a three-point bending test

The settings on the Hounsfield testing machine were as follows: load = 500 N, extension range = 50 mm, speed = 3 mm/min, span = 205 mm, end point = 45 mm, pre-load = 0 N and auto return on. The results were obtained as follows:
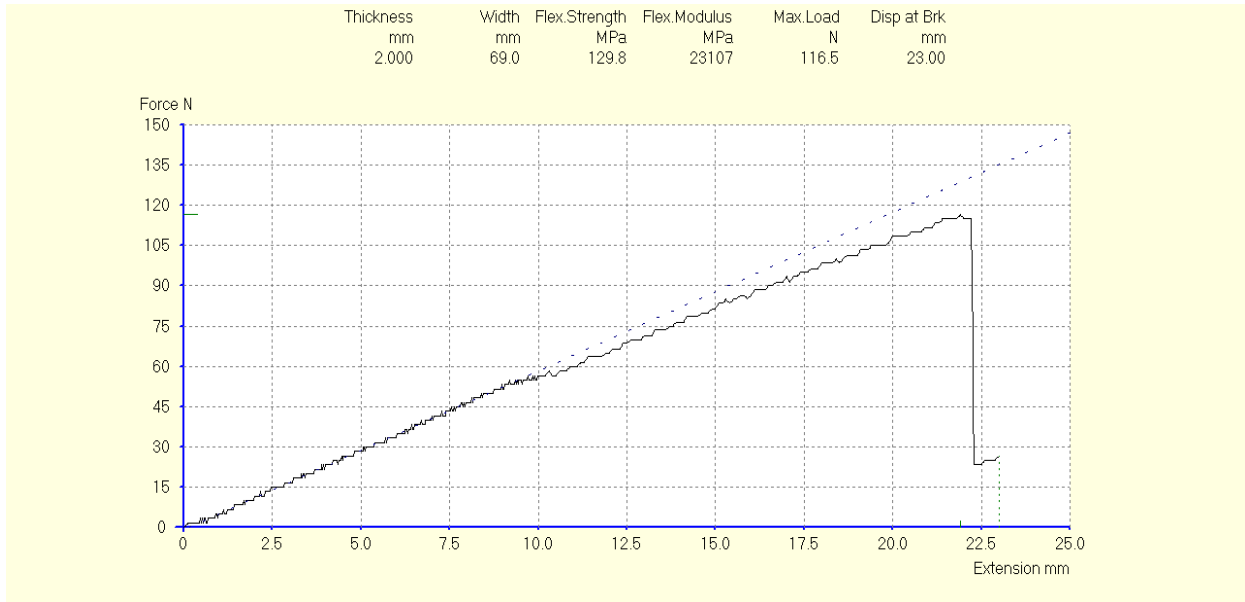
Figure 3.4: Results of sample A
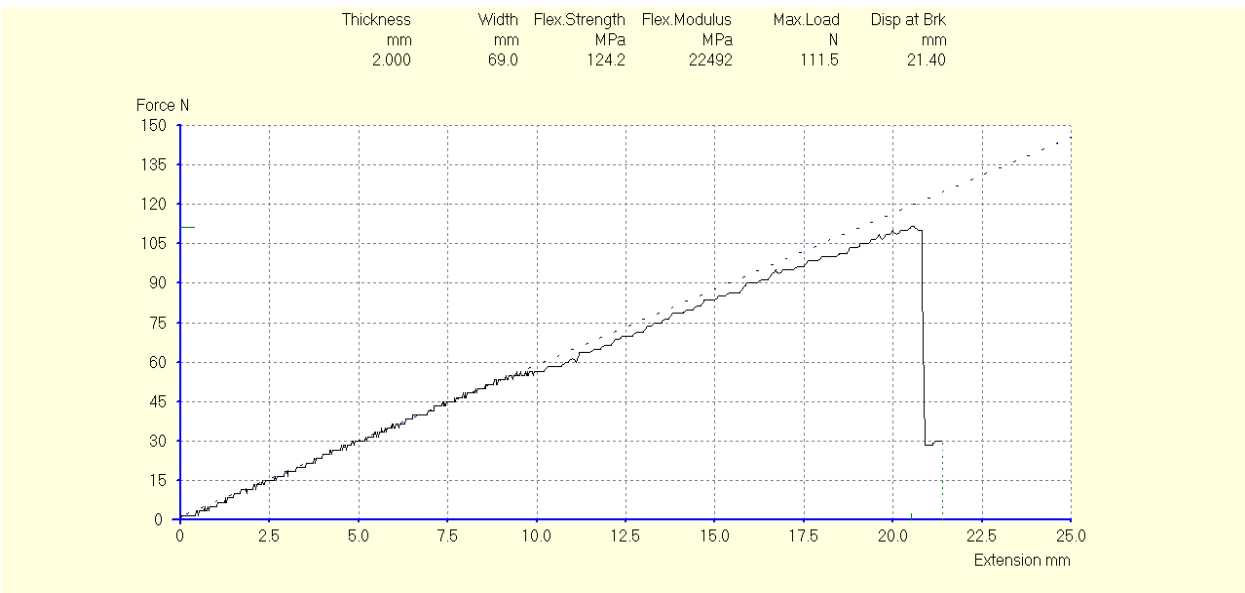
Figure 3.5: Result of sample B

	Thickness mm	Width mm	Flex.Strength MPa	Flex.Modulus MPa	Max.Load N	Disp at Brk mm
	2.000	69.0	118.7	22019	106.5	21.30
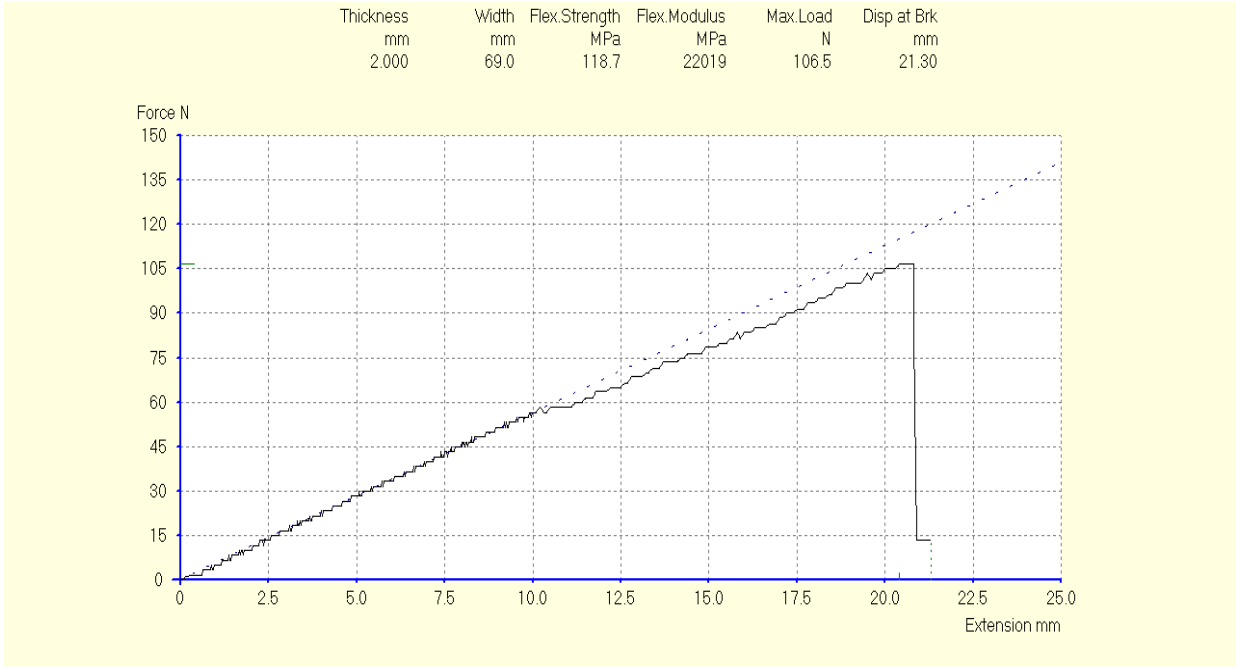
Figure 3.6: Results of sample C

	Thickness mm	Width mm	Flex.Strength MPa	Flex.Modulus MPa	Max.Load N	Disp at Brk mm
	2.000	69.0	132.0	22871	118.5	22.20
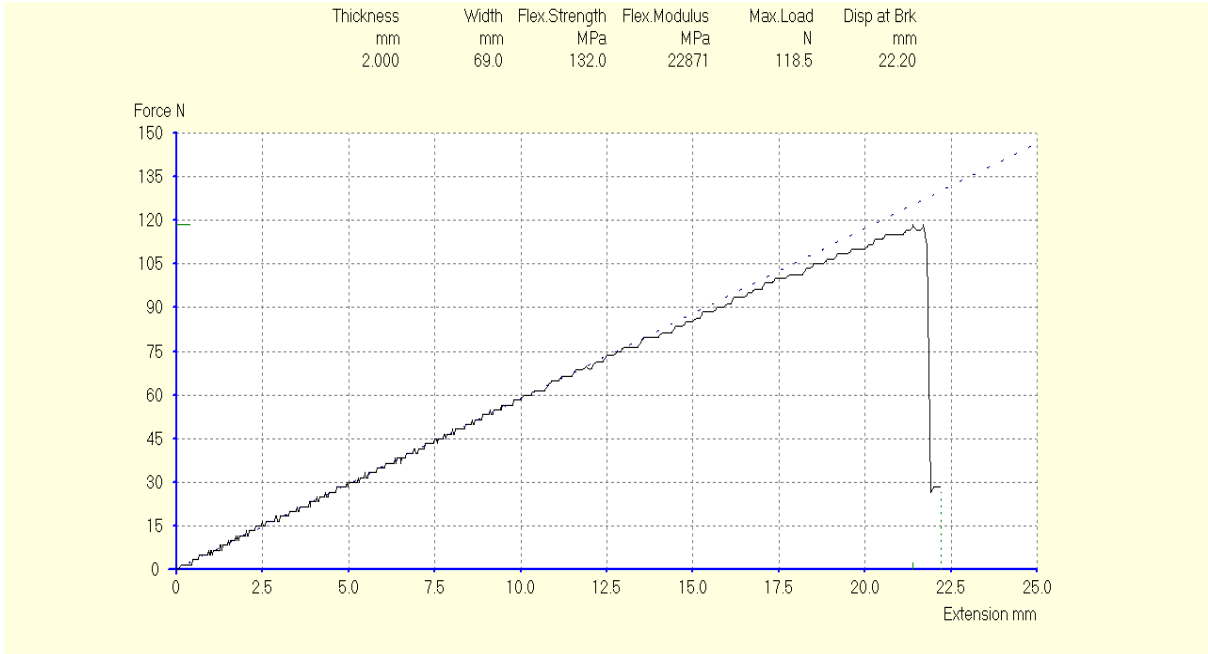
Figure 3.7: Results of sample D

On failure of the specimen, the Hounsfield recorded an average force (F) of 113 N and the average deformation (d) of 22 mm. To determine the E, I and σ value the following calculations were performed [22].

$$\sigma = \frac{My}{I}$$ Equation 3.3

$$\delta = \frac{FL^3}{48EI}$$ Equation 3.4

Equation 3.1 was used to calculate the maximum flexural stress of the specimen using the moment at the middle (*M*) and (*y*) for the neutral axis and (*I*) for the moment of inertia and in order to calculate the reaction force at the support, the following equation based on static mechanics was used.

$$\sum F_y = 0$$ Equation 3.5

And

$$\sum M_{@AnyPoint} = 0$$ Equation 3.6

Using equation 3.5 the following was obtained:

$$\sum F_y = -F + F_{Left-Support} + F_{Rigth-Support} = 0$$

$$\sum F_y = -113 + F_{Left-Support} + F_{Right-Support} = 0$$

Or

$$F_{Left-Support} + F_{Right-Support} = 113$$ Equation 3.7

Using equation 3.6 the following was obtained:

$$\sum M_{@Left-Support} = (-F * \frac{L}{2}) + (F_{Right-Support} * L) = 0$$

$$\left(-113 * \frac{0.2}{2}\right) + \left(F_{Right-Support} * 0.2\right) = 0$$

Solving for $F_{Right-Support}$ the following was obtained

$$F_{Right-Support} = \frac{\left(113 * \dfrac{0.2}{2}\right)}{0.2} = 56.5N$$

To calculate the value of the force on the left support, since the value of the right support was already obtained. The following substitution was made on equation 3.7.

$$F_{Left-Support} + 56.5 = 113$$

Therefore

$$F_{Left-Support} = 56.5N$$

In order to calculate the value of the moment acting at the midpoint and the value of the neutral axis the following equations were used:

*Moment = Σ Force * distance*

But in this case

$$M = F_{Right-Support} * \frac{L}{2}$$

$$M = 56.5 * 0.1 = 5.65 Nm$$

Then

$$y = \frac{h}{2} = \frac{0.002}{2} = 0.001m$$

An equation for solid rectangular cross section was used to calculate the moment of inertia (*I*)

$$I_{rec\tan gle} = \frac{bh^3}{12} = \frac{0.069 * 0.002^3}{12} = 4.6e^{-11}$$

Equation 3.1 was used to calculate the value of the maximum flexural stress of the specimen.

$$\sigma = \frac{My}{I} = \frac{5.65 * 0.001}{4.6e^{-11}} = 0.123 GPa$$

Rearranged equation 3.2, one can was able to calculate the Young's modulus of the material.

$$E = \frac{FL^3}{48\delta I} = \frac{113*0.2^3}{48*0.022*4.6e^{-11}} = 1.86 GPa$$

3.2 Digital Shearography System

This is a laser based optical Non-Destructive Testing system that can detect flaws in the composite structure which could occur at the manufacturing process or introduced to a structure during its service. The system consists of the Shearography head (1) mounted on a tripod (2), an industrial personal computer (3), carrying case (4). [23]

Figure 3.8: Digital Shearography [23]

The object to be studied is illuminated with an expanded beam from a point source of a laser and imaged by a shearing camera consisting of a Charge Couple Device (CCD) and an image

30

shearing device. The shearing device used is a modified Michelson interferometer, which splits one object point into two in the camera image plane. Consequently a pair of laterally sheared images is received by the image sensor.
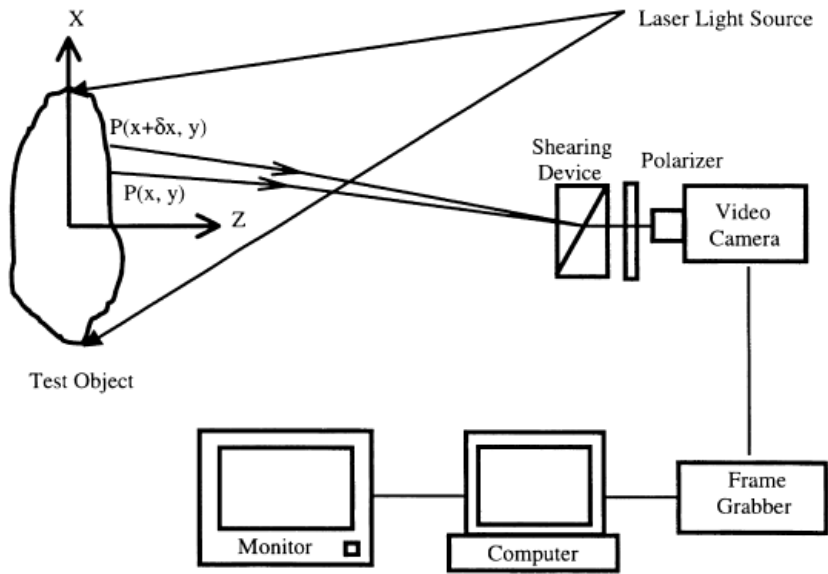
Figure 3.9: Fundamentals of Digital Shearography [24]

On the surface of the test object the speckle pattern will be produced due to a random interference and that pattern will be slightly altered when the object is deformed. That will be a stage when the desired shearing of the image has been attained and the digitizer will store it temporarily. The image that is stored on the digitizer will be the reference of which all the other speckle images produced will be compared to it and the results will be displayed on the monitor [24]. The object to be tested is stressed either by heat, pressure or any mechanical means. The flaws which distort the fringe pattern that is produced when comparing two speckled images are cracks, voids, delamination, corrosion etc.

3.2.1 Three-point bending test with the PVDF film sensor attached

Another set of samples were manufactured using the same procedure as the previous ones for determining the material properties. These samples had PVDF film sensor attached exactly in the middle using Q-bond adhesive, the PVDF sensor was 40 mm in length and was attached at 140 mm on each sample and four samples were cut. This experiment was performed to investigate a voltage spike produced due to sudden failure of the sample. This part was also to investigate the sensor to structure attachment because it is important to differentiate between the sensor and the structural failure.
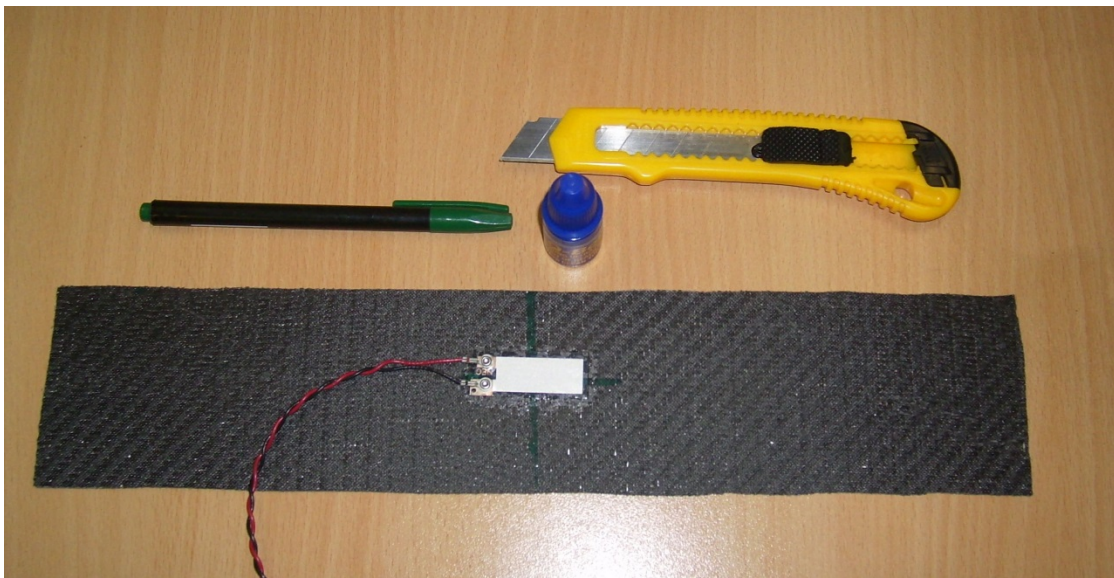
Figure 3.10: PVDF sensor attachment

The composite specimen with a PVDF film sensor attached in the mid-plane was tested in three-point bending as shown in figure 3.11 below.

Figure 3.11: Three-point bending test with PVDF sensor attached

The PVDF sensor was connected to a Fluke-View oscilloscope for data logging during the experiment. The aim of this experiment was to determine the voltage spike that the sensor produces at the point of fracture. The play back feature of the Fluke-View oscilloscope was used and then zoomed into the point of structural failure by putting a cursor at the point where maximum output of the sensor was recorded.

Figure 3.12: PVDF sensor attachment in a jig.

Fluke-View oscilloscope playback results of the attached PVDF sensor. Although the value of the voltage was meaningless but the experiment provided positive results that validated the concept of sensor to structural failure.

Four samples were tested in this experiment and the very same samples were tested on the next experiment where a Digital Shearography was used as stationery NDT to see if it could reveal the defects introduced by three-point bending test and also to understand how the Digital Shearography works. That experiment also revealed if the sensor was still intact to the structure after before and after failure.
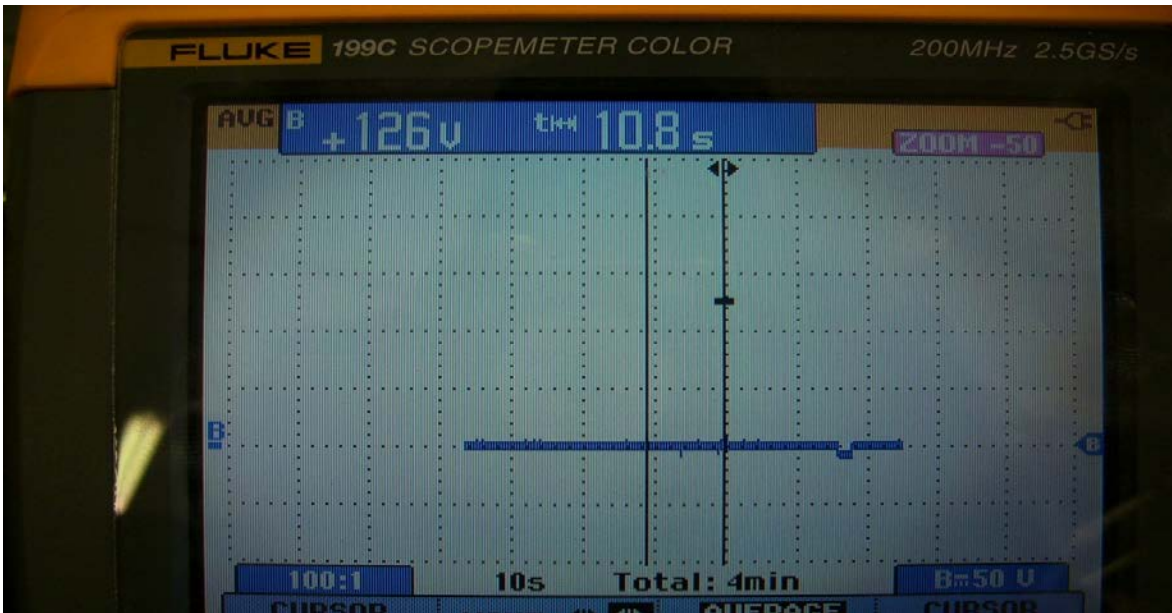
Figure 3.13: PVDF sensor output on sample A
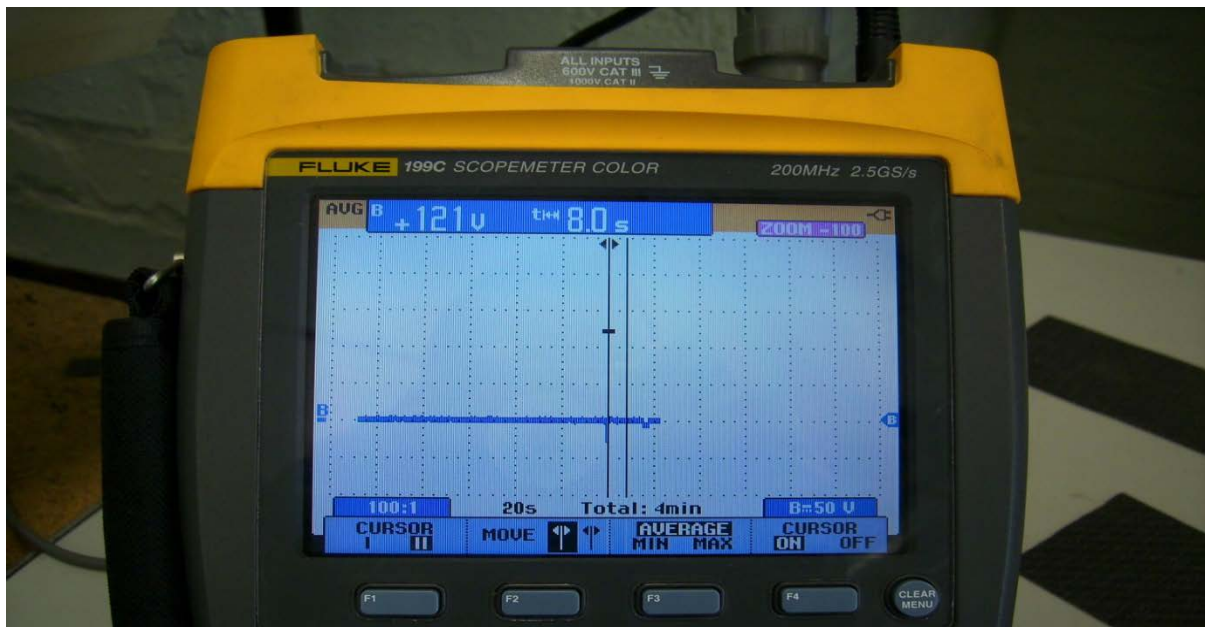
Figure 3.14: PVDF sensor output on sample B
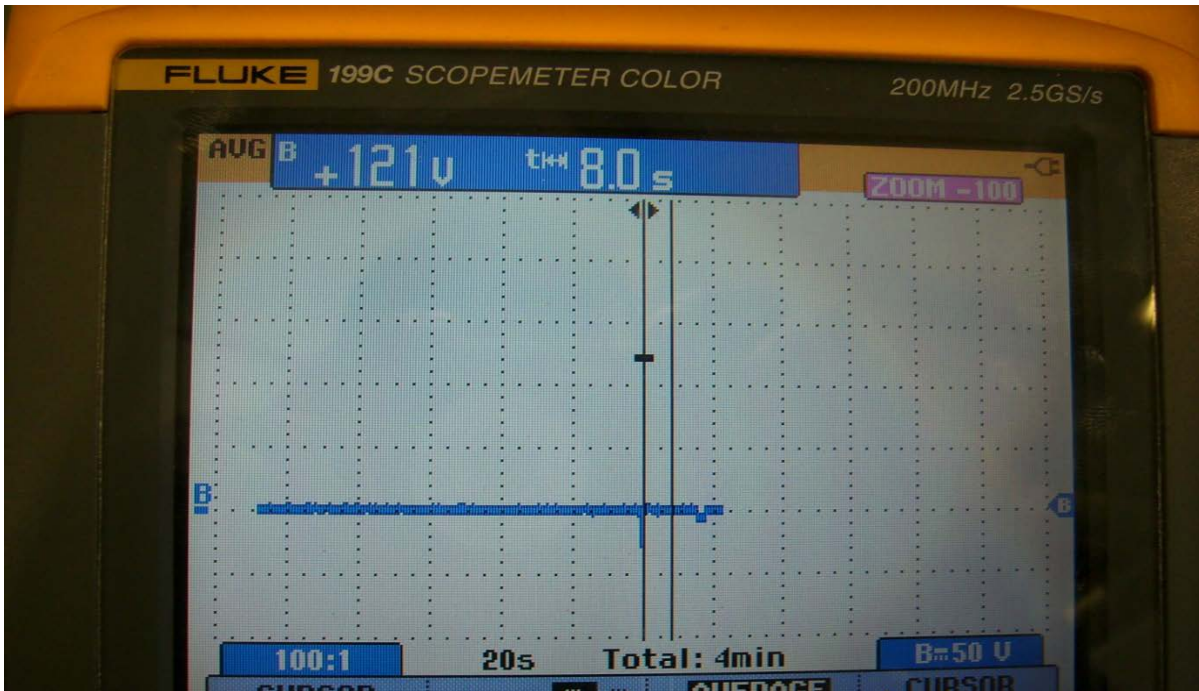
Figure 3.15: PVDF sensor output on sample C
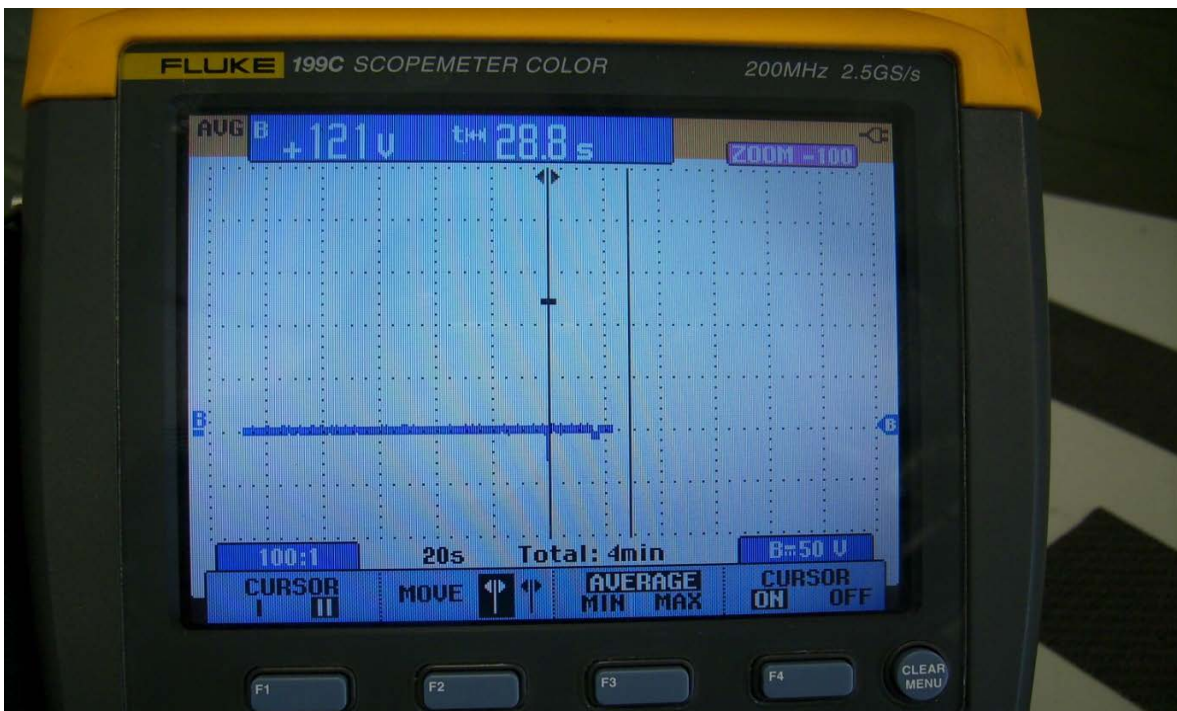
Figure 3.16: PVDF sensor output on sample D

36

The scale was set to 100:1 as seen from the screen; the majority of the specimens gave a maximum PVDF sensor output of 1.21V.

3.2.2 Digital Shearography test

The experimental set up includes the composite laminate specimens which were fabricated in the laboratory and cut into exact identical sizes of 280 mm x 69 mm x 2 mm, a heat source (hair dryer, 1.9 - 2.1 kW) and the digital shearography prototype. The first sample was defect free and the other four samples contained induced defects, which were introduced during the three point bending test as the specimens were loaded until failure occurred. The defects that were introduced into the panel samples were observed when three-point bending test was performed.
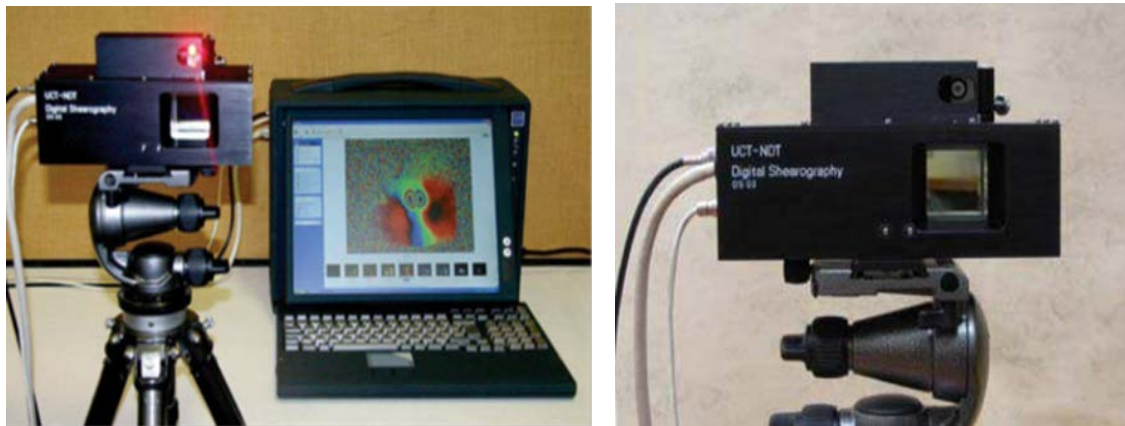
Figure 3.17: CPUT's portable Digital Shearography system [23]

The portable Digital Shearography system contains a phase stepper, a shearing optics, camera and a diode laser all contained in the head which is mounted on the tripod. The Shearographic "head" shown right in figure 3.17 above inspected the specimens that were positioned

horizontally on the laboratory table. The Sherographic head was linked to the personal computer that has its own software to control the Shearographic data acquisition for test results. The experiment test procedure began by illuminating a test specimen with the laser and viewed through an optical shearing device resulting into a sheared image. The image was captured and stored in the computer in its unstressed state. The digital Shearography software was then set into real-time mode to capture the test sample's behaviour when stressed thermally by warm air from a hair dryer for approximately five seconds. The user observed the object from the start of the heating and the cooling process.

The decision was made when to freeze/store the image pattern in the computer during the cooling process that revealed the presence of defects. The defects on all mildly stressed composite panels were identified by the abrupt changes in orientation or number of fringes in the interference pattern. The results of the inspection can be seen in the following figures that depict the fringe pattern obtained from the defect free samples as well as defected samples.

Figure 3.18: Defect free panel sample

38
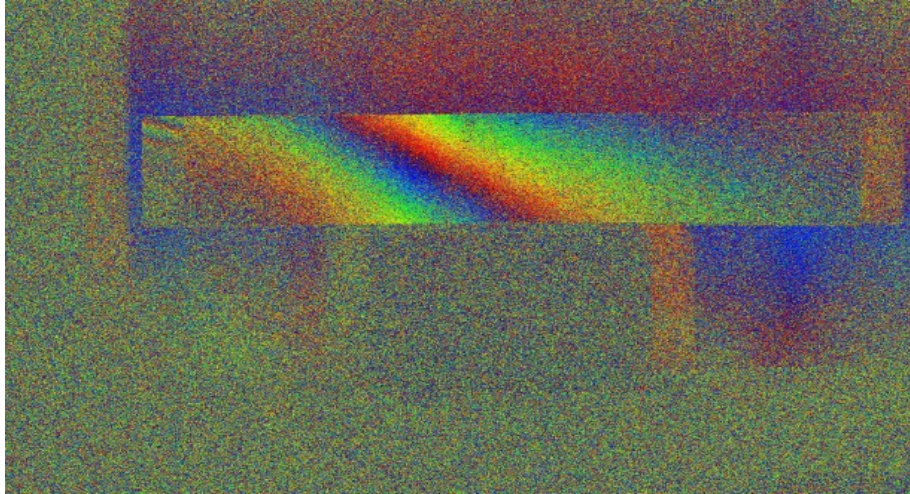
Figure 3.19: Phase stepped image result of defect free sample

The defects (the crack on one surface of the beam) on the following figures (3.20 to 3.27) were detectable by the localized fringes that appear in the interference pattern produced by the digital shearography technique on the surface directly opposite the position of the known defects. Illumination, thermal stressing and observation of the beam was effected with the crack (defect) placed in the far surface of the beam.
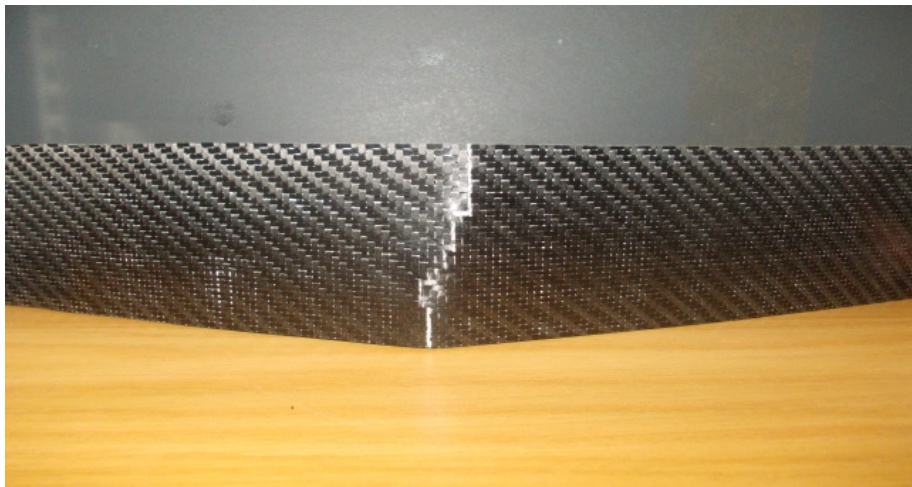
Figure 3.20: Specimen A
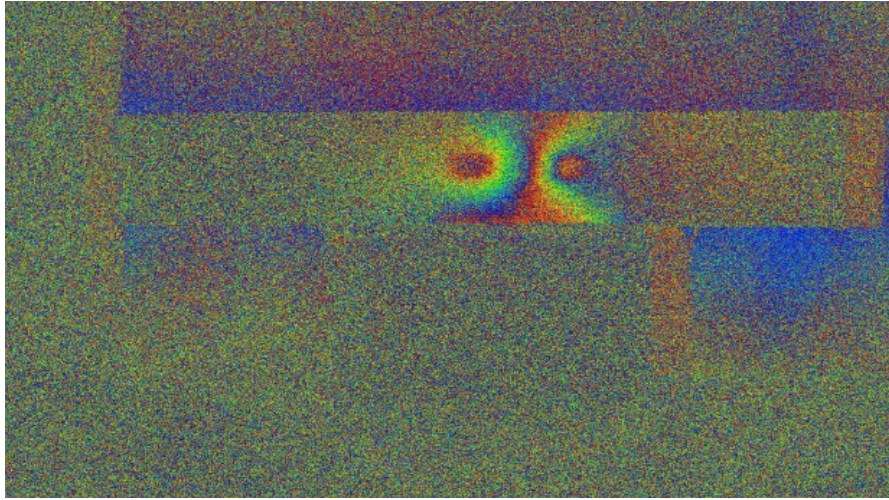
Figure 3.21: Phase stepped image results of sample A
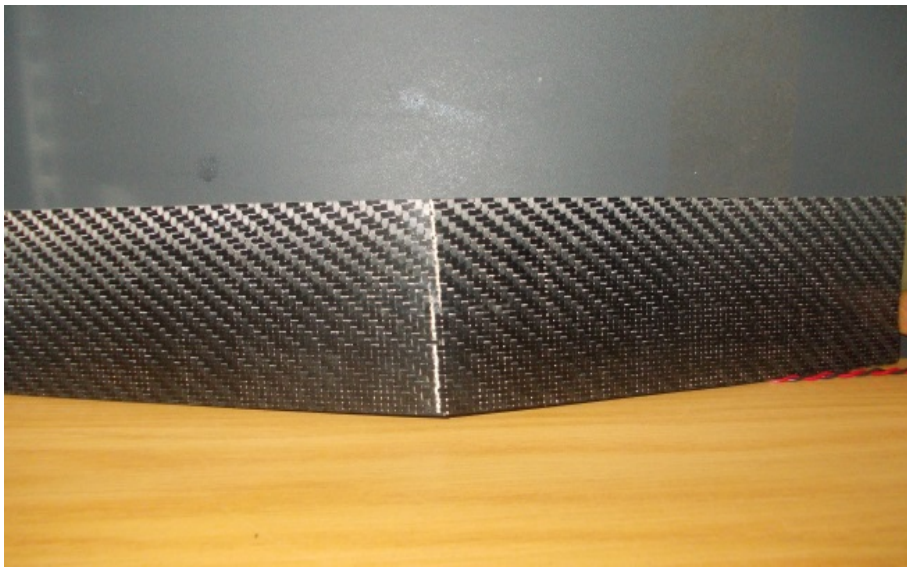
Figure 3.22: Sample B
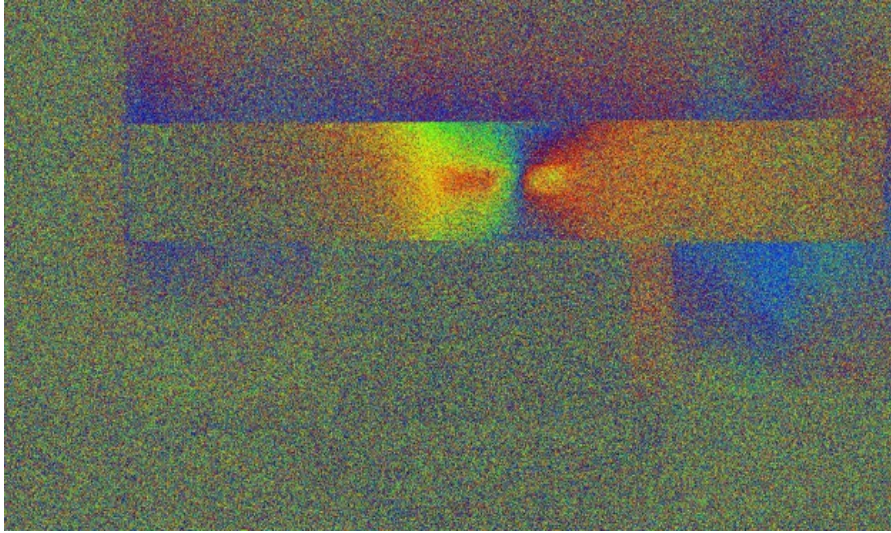
Figure 3.23: Phase stepped image results of sample B
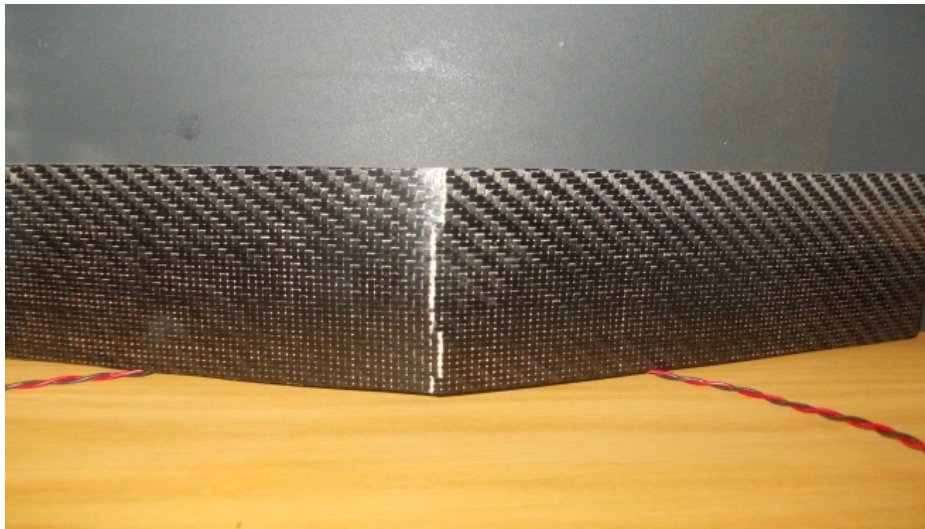
Figure 3.24: Sample C
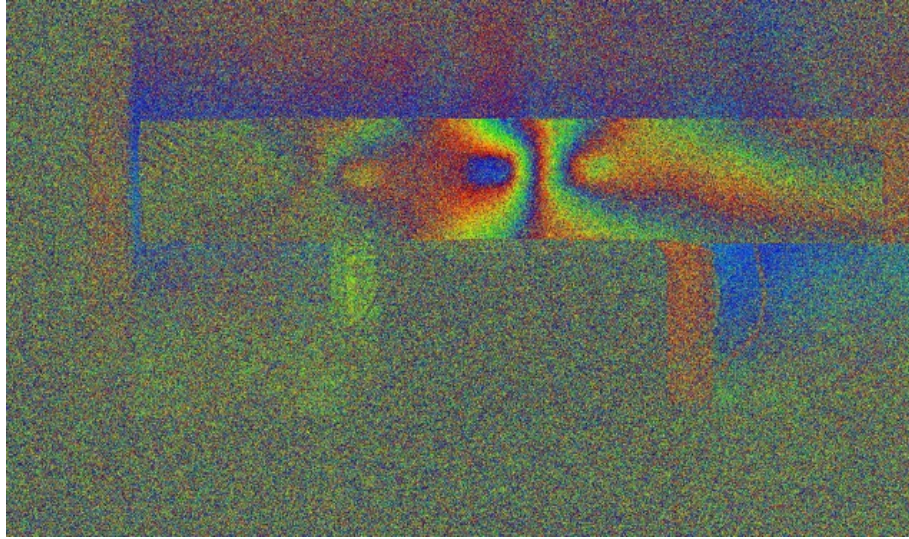
Figure 3.25: Phase stepped image results of sample C
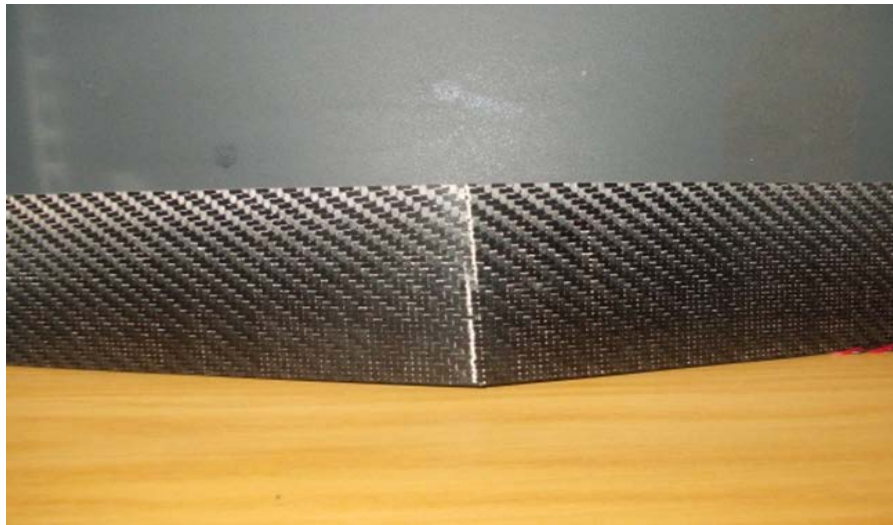
Figure 3.26: Sample D
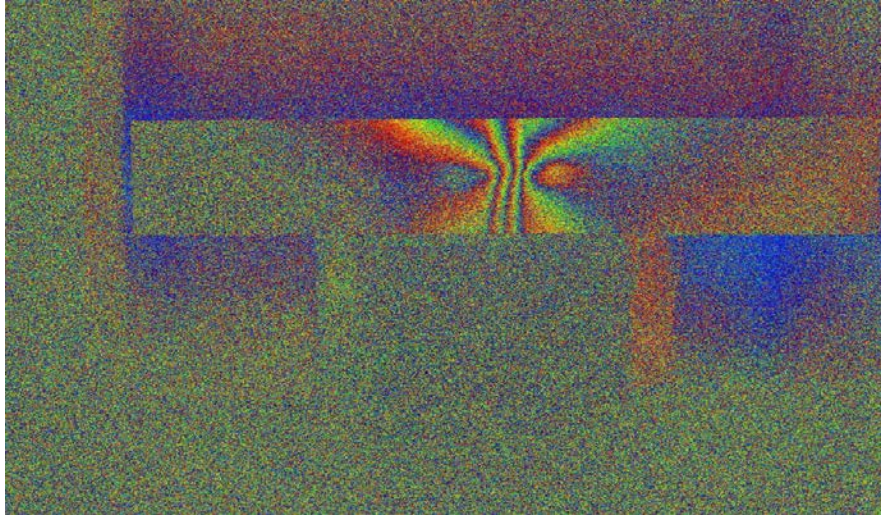
Figure 3.27: Phase stepped image results of sample D

The Digital Shearography results showed that there was the defect in a form of a crack in the samples, looking at the fringe pattern and also revealed the position but the structure must be stationery for scanning which is a limitation for this project.

Chapter four

4. Experimental investigation using PVDF sensor

This chapter looks at the experimental investigation using PVDF sensor to resemble the bending load introduced to the beam samples in a cantilever set-up. A set of five beam samples were manufactured using the same technique as in chapter 2 so that they have the same material properties. The four samples had a known defect of a 3 mm through hole drilled on it and one was defect free, which was the one used as a reference sample. The temperature effect was neglected as the experiment was conducted at room temperature.

4.1 Embedded PVDF sensor experiment

The main purpose of this experiment was to use the attached PVDF sensor as the sensing device to detect the adverse changes in the beam structure due to the presence of defects/flaws.

Samples were cut using a diamond saw; the dimensions of the samples were 280 mm x 69 mm x 2 mm. Each sample was clamped at 50 mm on one end as a cantilever beam. Measurements of displacement at the free end of specimen were obtained with the aid of a digital vertical Vernier scale.

The vertical Vernier scale tip was brought in to contact with the free end tip of the specimen. A mark at the tip free end of all specimens was made exactly at the same distance to serve as the tip contact point. Mass-pieces at the size of 50 g, 100 g, 150 g, 200 g, 250 g, 300 g, 350 g, 400 g and 450 g respectively were applied while measuring the displacement or deflection at the free end as the point load increases. The measurements were repeated several times but three sets of each

test were recorded to ensure consistency in results. One specimen was tested with no defect on it so as it was going to serve as the reference point for undamaged structure; defects were introduced at 50 mm, 100 mm , 150 mm and 200 mm from the fixed end and measurement of deflection were recorded. The flaws were introduced by drilling a 3 mm through hole into the specimen's centre-line. The aim was to produce a set of deflection values to be used when conducting the vibrational loading test. The PVDF sensor was connected to a Fluke-View oscilloscope and the data was stored in a computer using a data logging feature of the oscilloscope.

From literature, the characteristics of a PVDF sensor outlines that it is not suitable for static load measurements. When the beam samples were loaded, the mass pieces were let to impact the sample and it will deflect and vibrate until it settles but with the mass piece will still be attached as a point load and that was the point of interest because it was where the sensor gave a maximum voltage output and maximum deflection for that added load. The mass pieces were released at minimal height so as to ensure the stacking and not to fall off the beam sample loading point. Measurements of the maximum deflection were only taken at a point when the sample was stationery. Time domain measurements option was used because it allows for measurement of deflection as amplitude in volts (V) of the periodic wave form generated due to loading of the beam sample.

4.1.1 Deflection and voltage measurements result

As the damage moved closer to the fixed end of the specimen, it resulted in higher free end displacement that indicated reduced apparent bending stiffness (*EI*). This demonstrated as

45

expected that the stress discontinuity introduced by the defect influence the bending stiffness of the beam. Displacements for the different applied loads indicated a linear relationship between them as shown in the following results. The following were the results as the impact load measurements were recorded and analysed using an Excel spreadsheet. The defect position was measured from the fixed end of the sample. A trend-line was used in the analysis of the results and it showed the relationship between the load and the displacement due to the presence of the flaw in a structure and also to produce an equation of a straight line since the relationship was linear.

Table 1: Defect Free Beam, a = 0 (Beam 0)				
Load (N)	Y_1 (mm)	Y_2 (mm)	Y_3 (mm)	Average (mm)
0	0	0	0	0.00
0.49	0.63	0.68	0.65	0.65
0.98	1.3	1.39	1.4	1.36
1.47	2.3	2	2.4	2.23
1.96	3.4	3.72	3.5	3.54
2.45	4.9	5.1	4.91	4.97
2.94	6.12	6.1	5.99	6.07
3.43	7.22	6.9	7	7.04
3.92	7.86	7.8	7.95	7.87
4.41	8.59	8.62	8.63	8.61
Table 2: Defect position, a = 50 mm (Beam A)				
Load (N)	Y_1 (mm)	Y_2 (mm)	Y_3 (mm)	Average (mm)
0				0.00
0.49	0.95	1.2	0.99	1.05
0.98	1.96	2	2.3	2.09
1.47	3.2	2.99	3.1	3.10
1.96	4.5	4.52	4.52	4.51
2.45	6.42	6.5	6.55	6.49
2.94	7.95	8.2	8.31	8.15
3.43	9.56	9.5	9.6	9.55
3.92	10.63	10.6	10.58	10.60
4.41	11.89	12.34	12.1	12.11
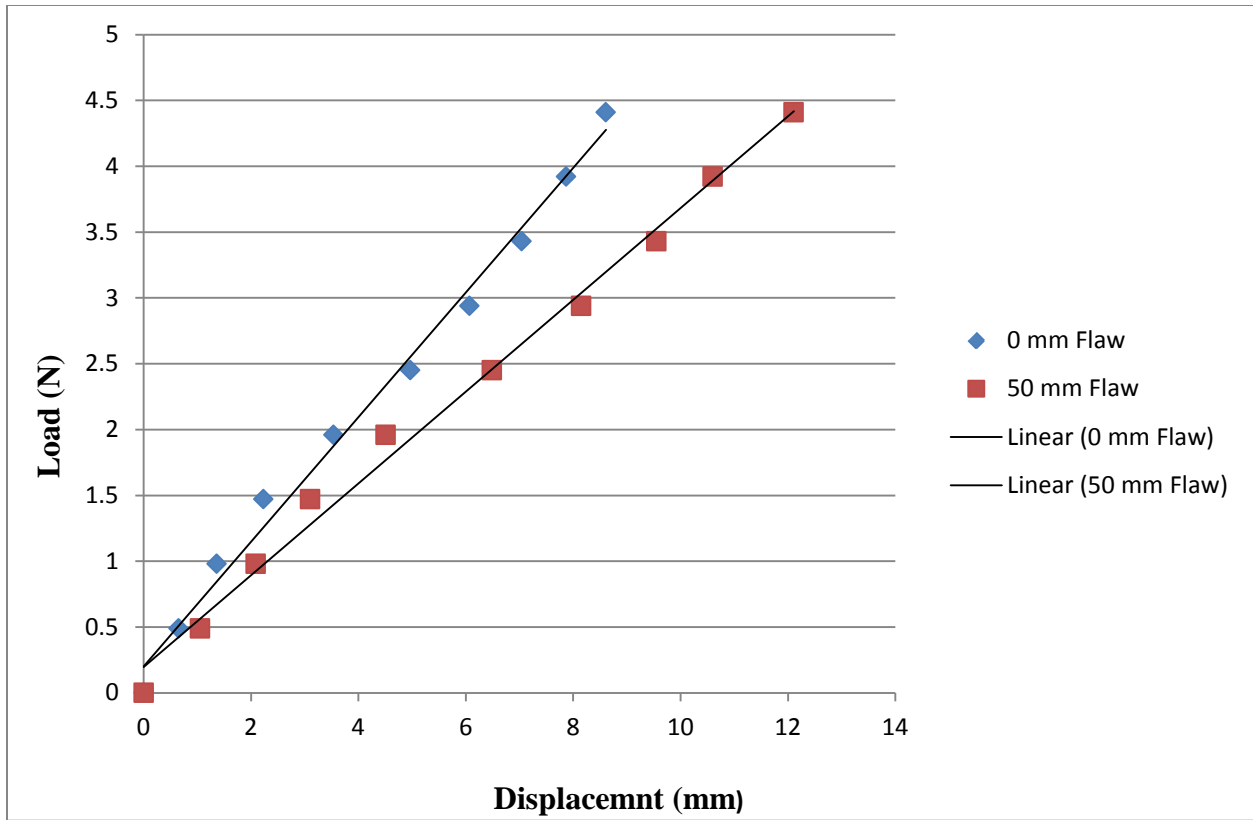
Figure 4.1: Load vs displacement for flawed beam at a = 50 mm

Table 3: Defect position, a = 100 mm (Beam B)				
Load (N)	Y_1 (mm)	Y_2 (mm)	Y_3 (mm)	Average (mm)
0	0	0	0	0.00
0.49	0.82	0.83	0.82	0.82
0.98	0.98	0.99	1.1	1.02
1.47	2.61	2.58	2.57	2.59
1.96	3.53	3.57	3.6	3.57
2.45	4.97	4.97	4.98	4.97
2.94	6.1	6.13	6.12	6.12
3.43	7.67	7.77	7.78	7.74
3.92	8.99	9.25	9.15	9.13
4.41	10.82	10.79	10.83	10.81
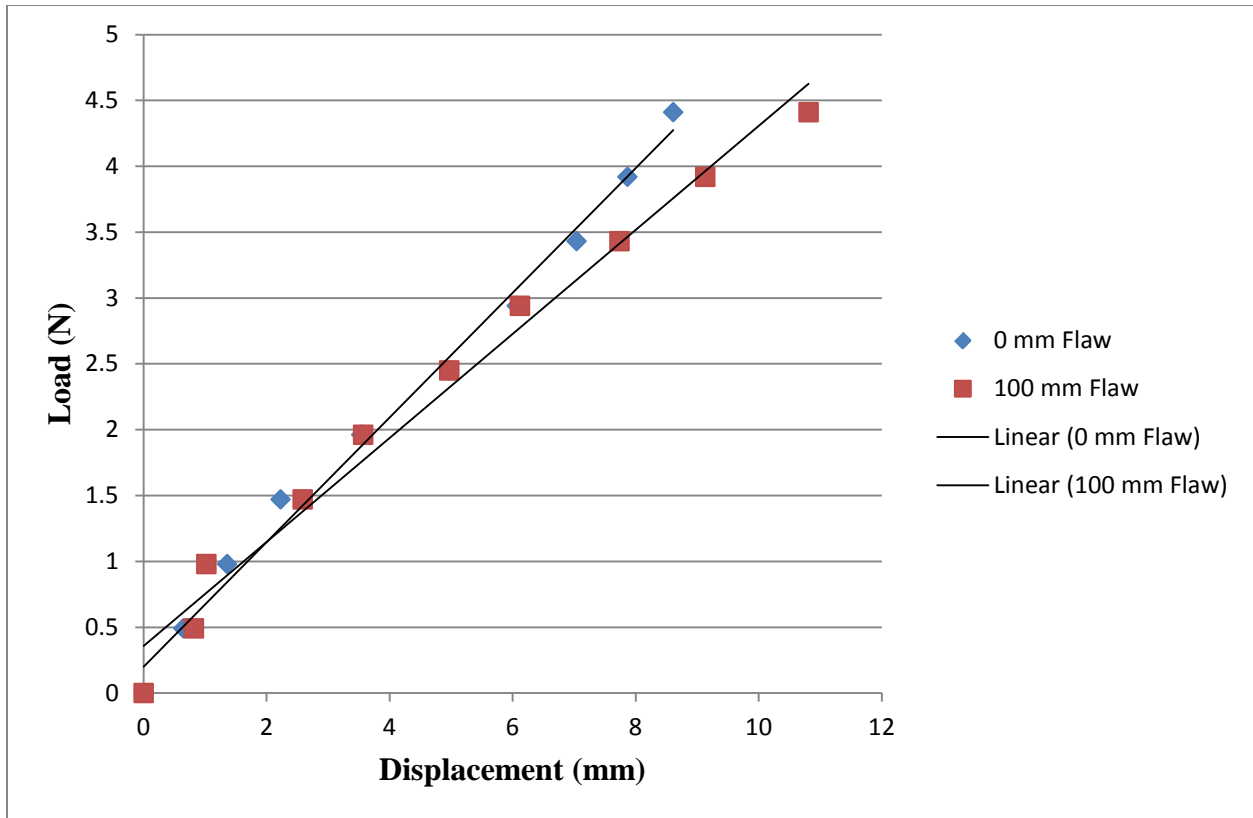
Figure 4.2: Load vs displacement for flawed beam at a = 100 mm

Table 4: Defect position, a = 150 mm (Beam C)				
Load (N)	Y_1 (mm)	Y_2 (mm)	Y_3 (mm)	Average (mm)
0	0	0	0	0.00
0.49	0.76	0.8	0.81	0.79
0.98	1.11	1.1	1.12	1.11
1.47	2.51	2.57	2.6	2.56
1.96	3.58	3.47	3.56	3.54
2.45	4.97	4.9	4.46	4.78
2.94	6.2	6	5.98	6.06
3.43	7.84	7.8	7.69	7.78
3.92	8.65	8.5	8.55	8.57
4.41	9.2	9.25	9.34	9.26
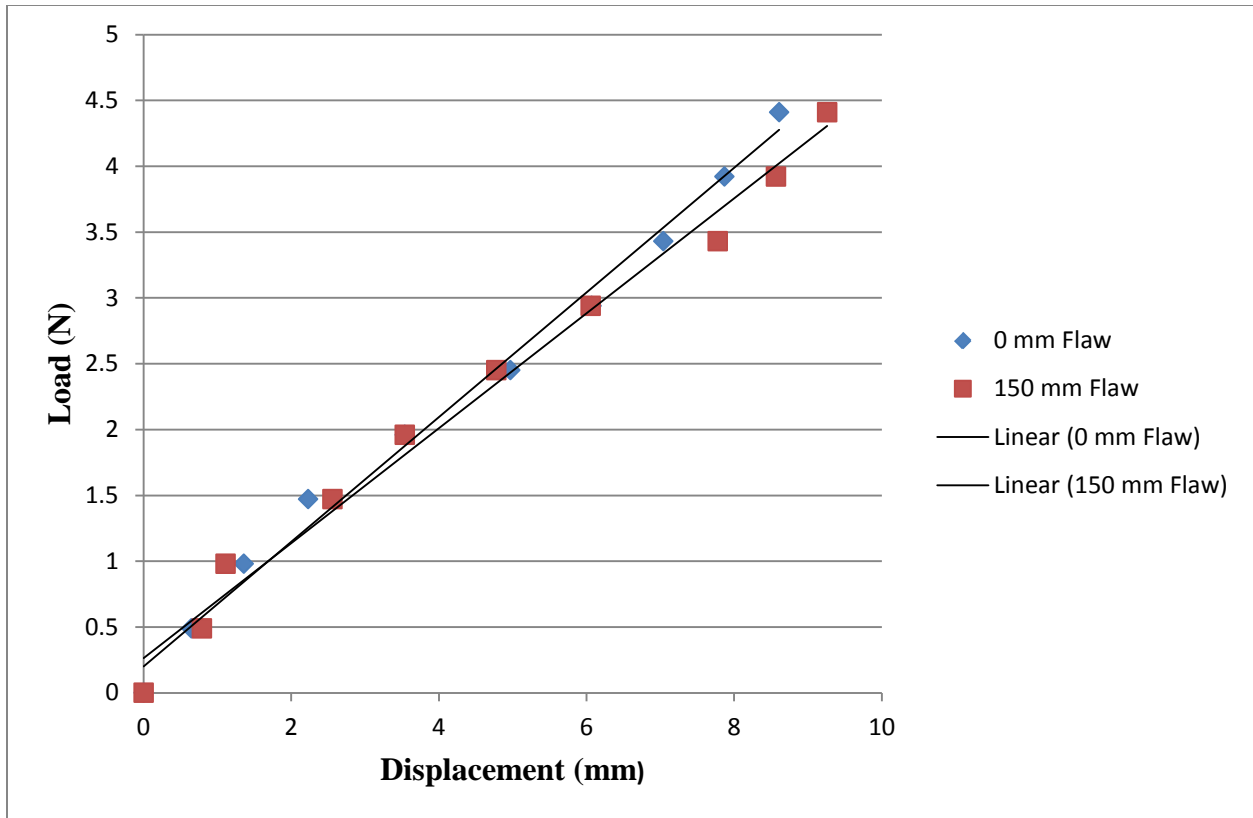
Figure 4.3: Load vs displacement for flawed beam at x = 150 mm

Table 5: Defect position, a = 200 mm (Beam D)				
Load (N)	Y_1 (mm)	Y_2 (mm)	Y_3 (mm)	Average (mm)
0	0	0	0	0.00
0.49	0.66	0.68	0.6	0.65
0.98	1.64	1.67	1.66	1.66
1.47	2.71	2.68	2.7	2.70
1.96	3.72	3.62	3.86	3.73
2.45	4.92	5.1	4.91	4.98
2.94	5.9	6.1	5.99	6.00
3.43	7.22	6.9	7.21	7.11
3.92	7.77	7.8	7.95	7.84
4.41	8.59	8.62	8.63	8.61
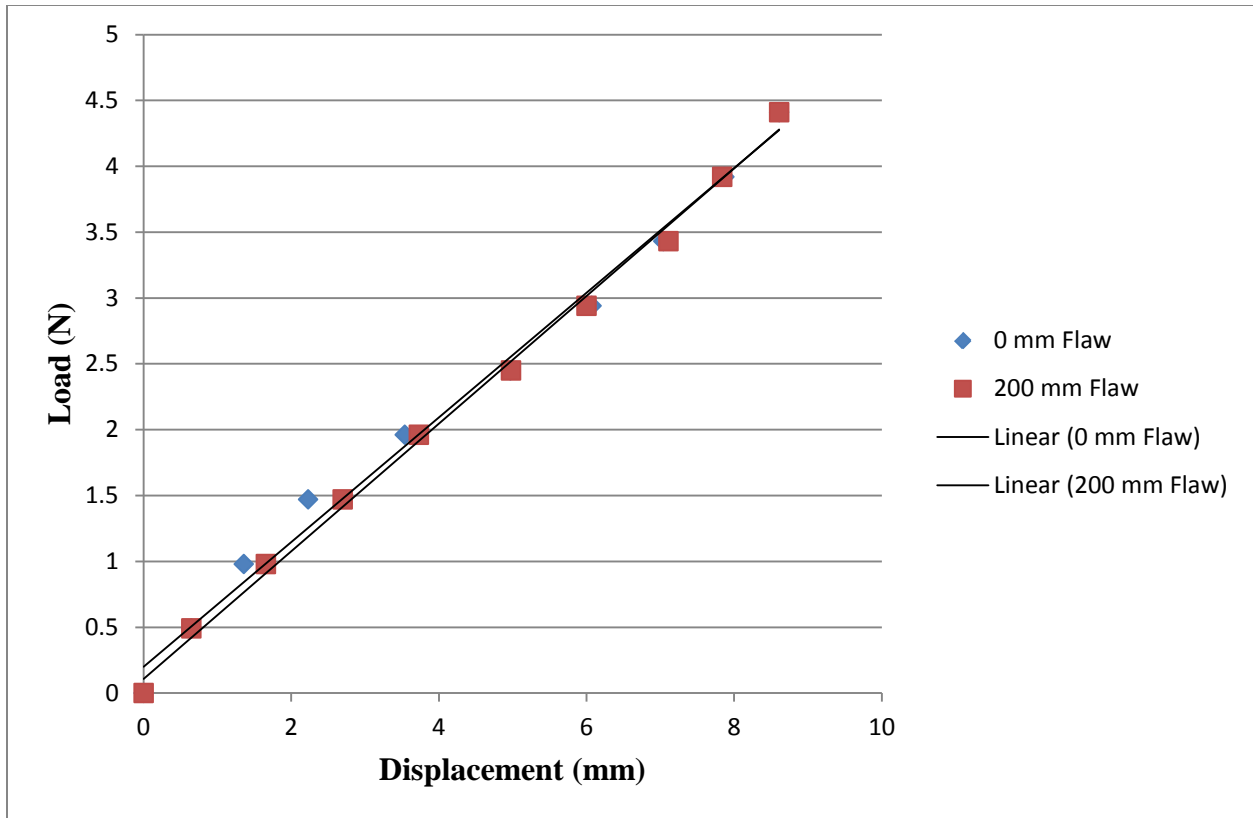
Figure 4.4: Load vs displacement for flawed beam at a = 200 mm

Measurements of the PVDF sensor output were also taken at the same instant of displacement results using a data logging feature of a Fluke-View oscilloscope connected to a dedicated computer. This was also done to obtain the deflections results that would be used when the beam sample was loaded using a vibration load. Experimental measurements of the PVDF sensor's output voltage for a free end displacement under the impact loading were recorded and the PVDF sensor recorded a voltage spike each time a mass piece was added. For each sample, a set three readings were obtained to ensure consistency and an average value of the output voltage was used to analyse the results.

PVDF sensor output for impact loading (V)

Table 6: Damage position, a = 0 (Beam 0)				
Load (N)	V_1	V_2	V_3	Average (V)
0	0	0	0	0.00
0.49	0.29	0.31	0.29	0.30
0.98	0.73	0.8	0.69	0.74
1.47	1.2	1.34	1.31	1.28
1.96	2.24	2.08	2.44	2.25
2.45	3.41	3.28	3.22	3.30
2.94	3.94	3.6	3.78	3.77
3.43	4.7	4.62	4.68	4.67
3.92	5.4	5.35	5.61	5.45
4.41	5.92	5.91	5.9	5.91

Table 7: Damage position, a = 50 mm (Beam A)				
Load (N)	V_1	V_2	V_3	Average (V)
0	0	0	0	0.00
0.49	0.4	0.38	0.41	0.40
0.98	1.47	1.46	1.48	1.47
1.47	2.98	2.99	3	2.99
1.96	3.61	3.61	3.63	3.62
2.45	4.33	4.32	4.3	4.32
2.94	4.93	4.92	4.93	4.93
3.43	5.8	5.72	5.74	5.75
3.92	6.22	6.22	6.18	6.21
4.41	6.93	6.94	6.88	6.92
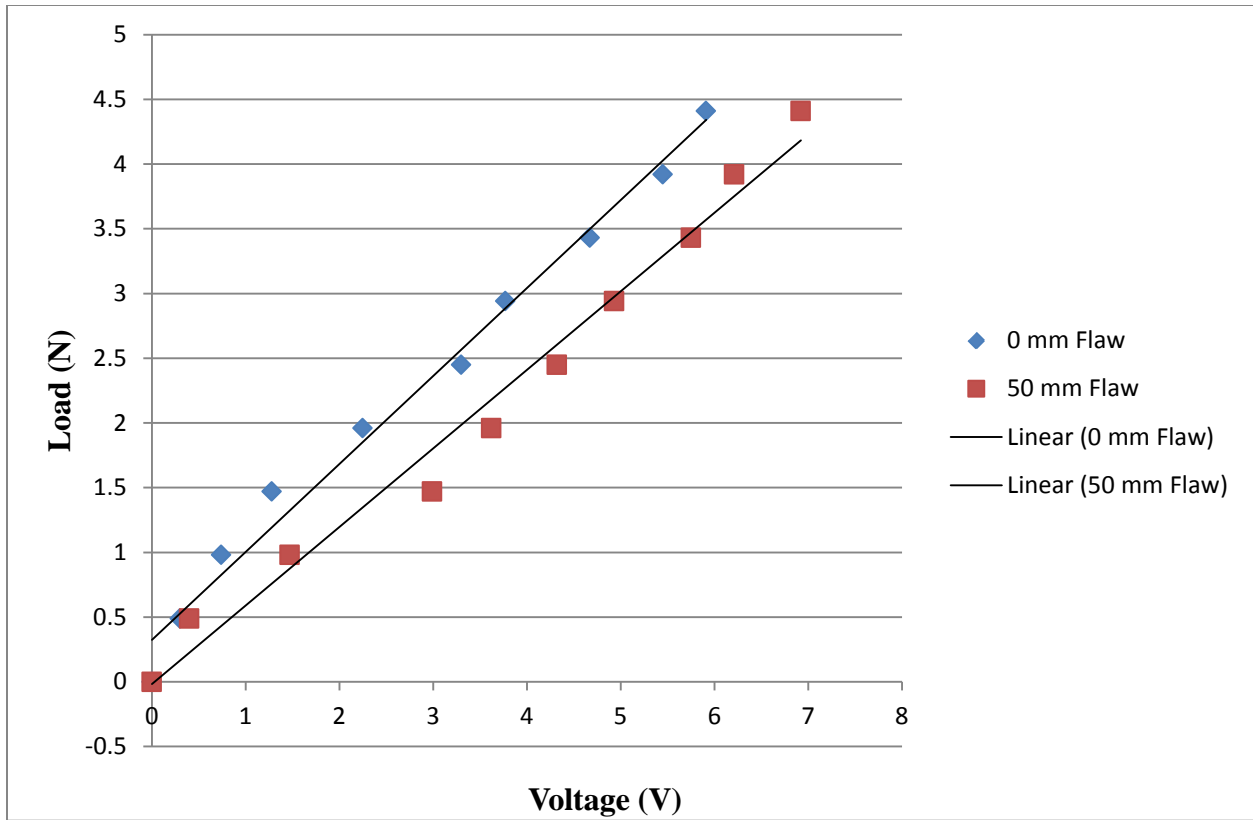
Figure 4.5: Load Vs Voltage for flawed beam at a = 50 mm

Table 8: Damage position, a = 100 mm (Beam B)				
Load (N)	V_1	V_2	V_3	Average (V)
0	0	0	0	0.00
0.49	0.63	0.6	0.62	0.62
0.98	1.4	1.34	1.41	1.38
1.47	2.6	2.61	2.3	2.50
1.96	3.46	3.52	3.6	3.53
2.45	3.95	4.12	3.82	3.96
2.94	4.56	4.5	4.55	4.54
3.43	4.99	4.98	4.99	4.99
3.92	5.85	5.85	5.84	5.85
4.41	6.56	6.56	6.57	6.56
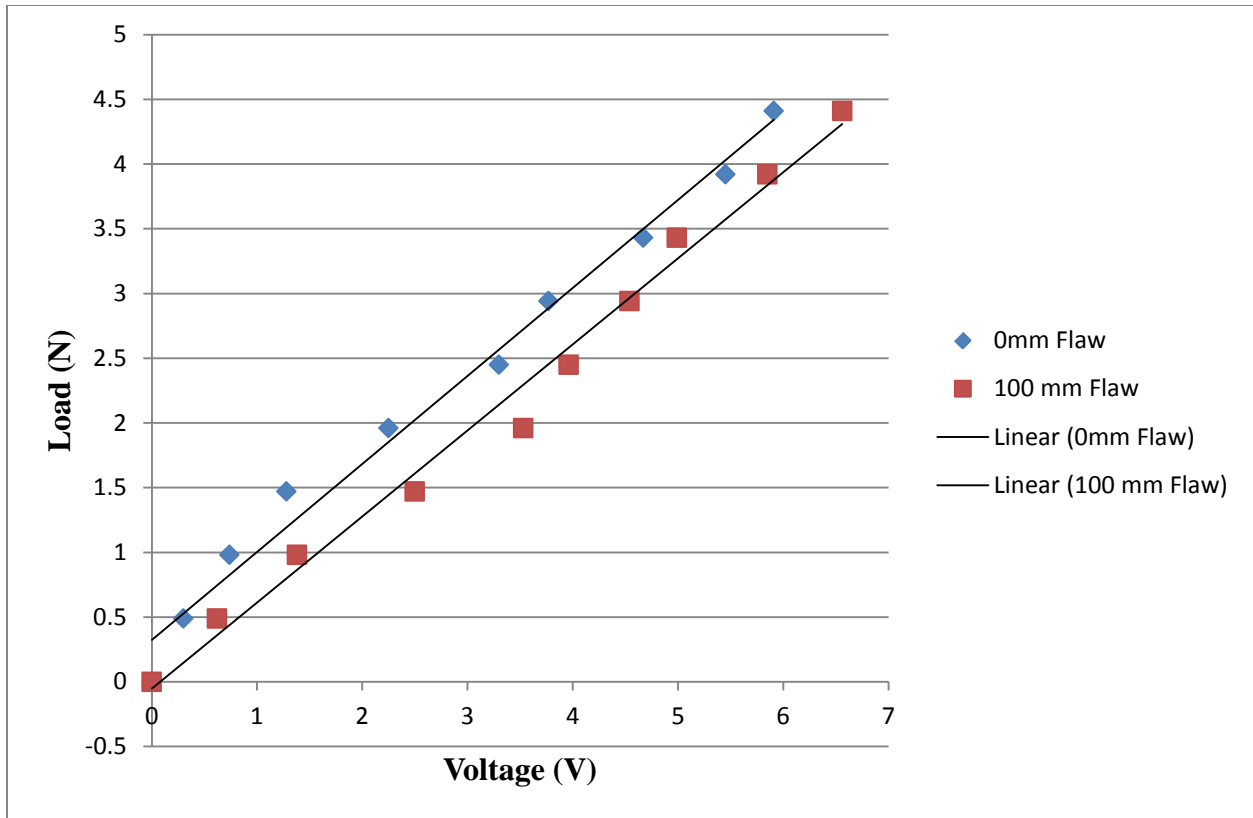
Figure 4.6: Load Vs Voltage for flawed beam at a = 100 mm

Table 9: Damage position, a = 150 mm (Beam C)				
Load (N)	V_1	V_2	V_3	Average (V)
0	0	0	0	0.00
0.49	0.45	0.5	0.45	0.47
0.98	0.99	0.96	0.98	0.98
1.47	1.45	1.44	1.45	1.45
1.96	2.6	2.54	2.57	2.57
2.45	3.46	3.44	3.42	3.44
2.94	4.23	4.2	4.2	4.21
3.43	4.51	4.5	4.36	4.46
3.92	5.24	5.21	5.24	5.23
4.41	6.32	6.2	6.14	6.22
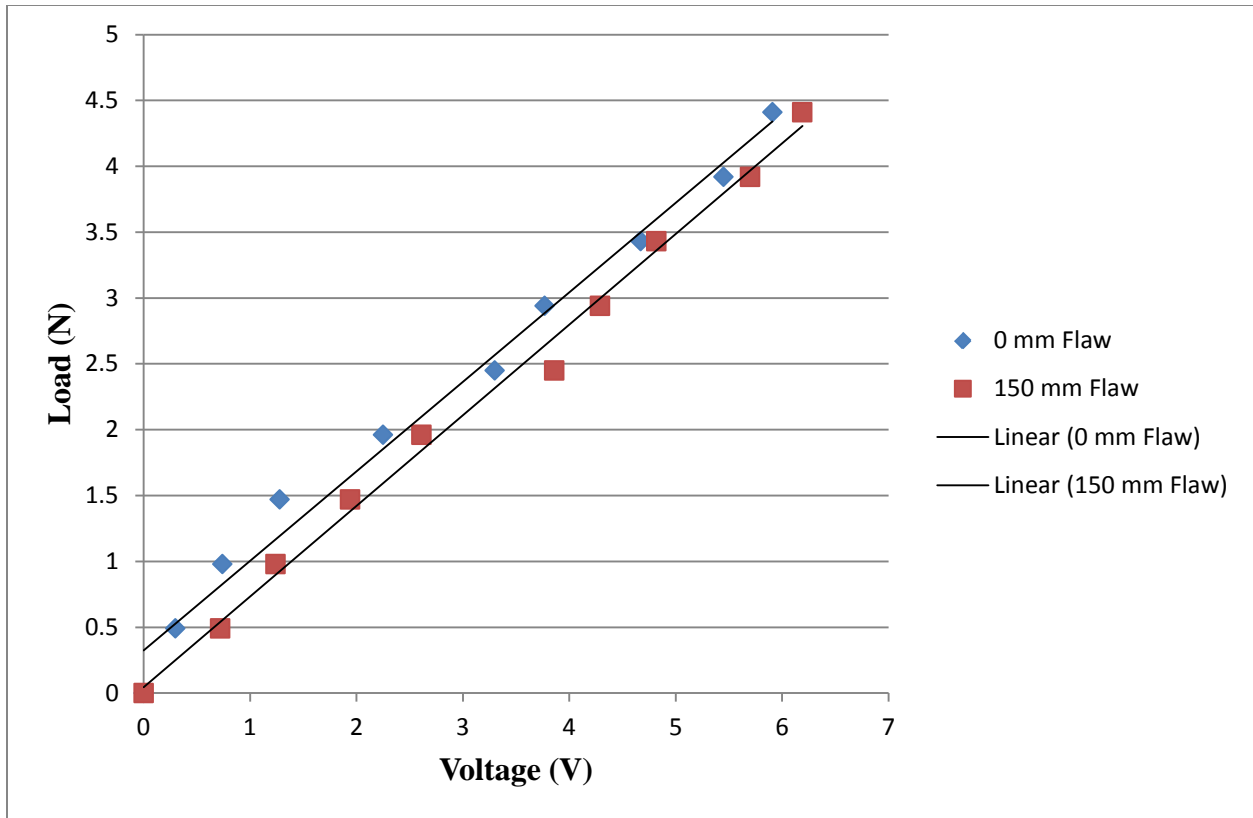
Figure 4.7: Load Vs Voltage for flawed beam at a = 150 mm

Table 10: Damage position, a = 200 mm (Beam D)				
Load (N)	V_1	V_2	V_3	Average (V)
0	0	0	0	0.00
0.49	0.69	0.75	0.73	0.72
0.98	1.2	1.22	1.3	1.24
1.47	1.96	1.86	1.99	1.94
1.96	2.62	2.54	2.67	2.61
2.45	3.86	3.84	3.88	3.86
2.94	4.27	4.3	4.29	4.29
3.43	4.78	4.84	4.83	4.82
3.92	5.72	5.7	5.68	5.70
4.41	6.18	6.2	6.19	6.19

54
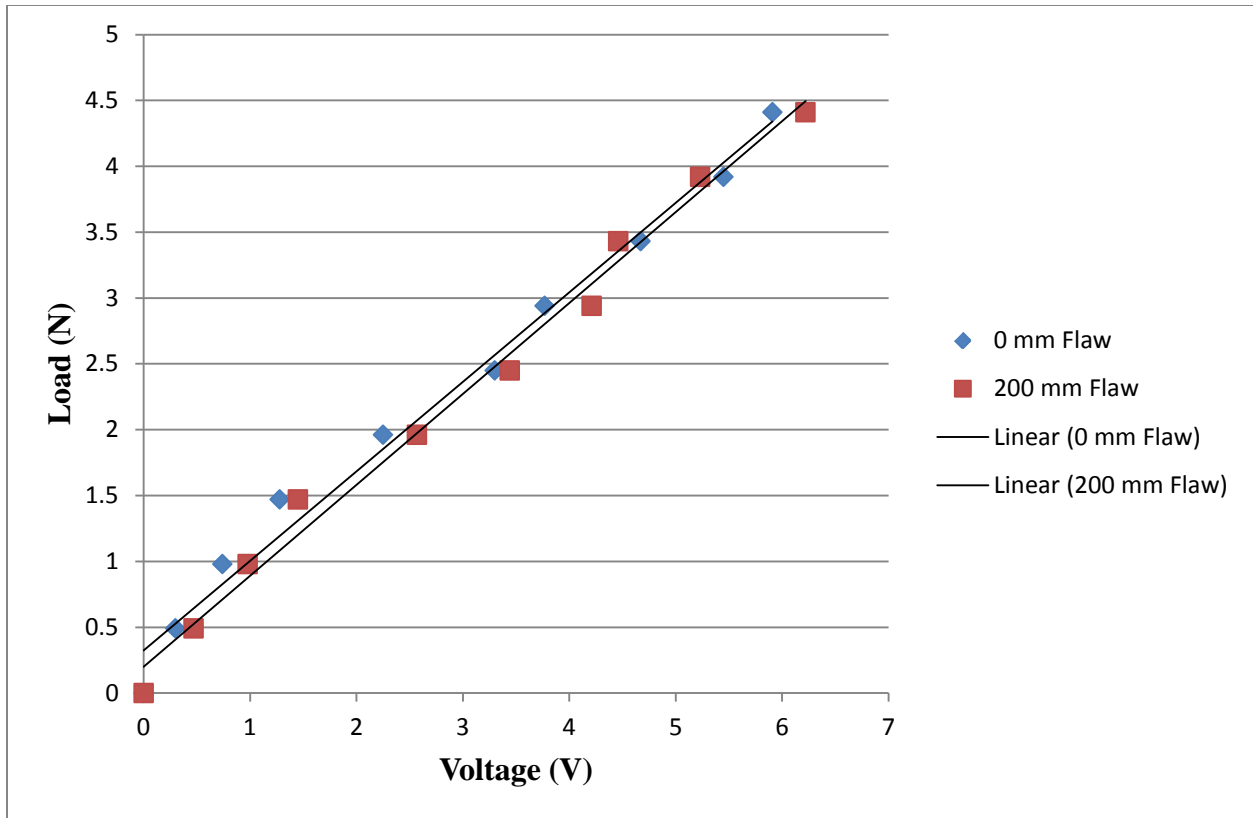
Figure 4.8: Load Vs Voltage for flawed beam at x = 200 mm

For a uniform cantilever beam (shown in figure 4.9), exhibiting elastic properties, being subjected to a load at the free end, the maximum deflection and slope is given respectively by:

$$y_{MAX} = \frac{PL^3}{6EI}$$
equation 4.1

and

$$\frac{dy}{dx}_{MAX} = \frac{PL^2}{2EI}$$
equation 4.2
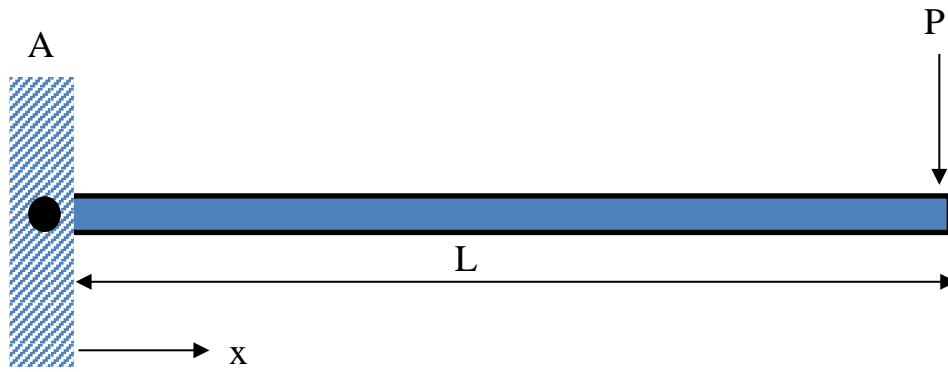
Figure 4.9: Cantilever beam (Mode 1)

Previous experimental results (figure 4.1 – 4.8) have shown that the introduction of a flaw caused an increase in the deflection and the sensor output voltage for similar free end loads due to the presence of a flaw. This investigation leads this study to the assumption that the flaw is caused by the presence of a virtual load P' then one can represent the cantilever described in figure 4.9 as:
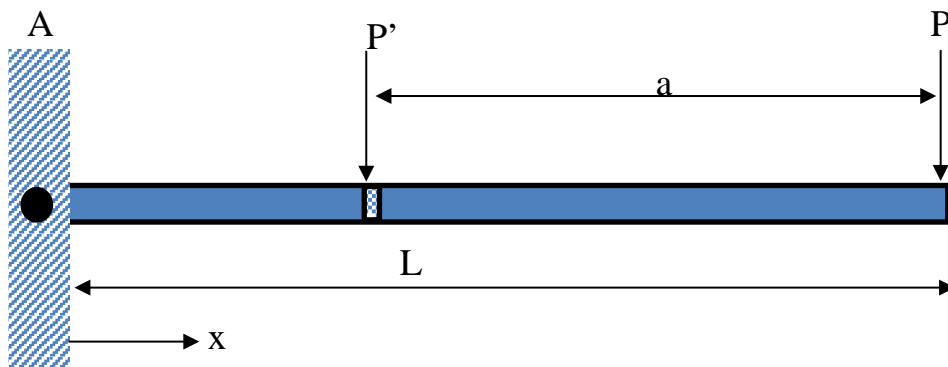
Figure 4.10: Cantilever beam virtual load (Mode 2)

This assumption was also investigated numerically using Macaulay's method as follows:

$$M_A = P_x = EI\frac{d^2y}{dx^2}$$

$$EI\frac{dy}{dx} = P\frac{x^3}{6} + C_1$$

$$EIy = P\frac{x^3}{6} + C_1 + C_2$$

Applying the boundary conditions:

at $x = 0, \frac{dy}{dx} = 0$ then $C_1 = 0$

at $x = 0, y = 0$ then $C_2 = 0$

But at

$$x = L$$
$$\left.\frac{dy}{dx}\right|_{max} = slope = \frac{PL^2}{2EI}$$
$$and$$
$$\left.y\right|_{max} = deflection = \frac{PL^3}{6EI}$$

That proves that for a healthy beam equation 4.1 and 4.2 are true, where a is the distance from the free end. When a flaw is introduced to a structure, it changes the deflection and thereby introducing a virtual load to a structure and this is true if the structure remains in its elastic form as in this study. The following numerical analysis was conducted to advocate this assumption. The free end deflection is then derived as follows:

$$\sum M_A = 0$$

Then

Moment: $\qquad M_A = EI\frac{d^2y}{dx^2} = Px + P'(x - a)$

Slope : $\qquad EI\frac{dy}{dx} = P\frac{x^2}{2} + P'\frac{(x-a)^2}{2} + C_1$

Deflection: $\qquad EIy = P\frac{x^3}{6} + P'\frac{(x-a)^3}{6} + C_1x + C_2$

57

The, applying boundary conditions,

$$x = 0 \ ; \frac{dy}{dx} = 0 \ \dots \ C_1 = -P' \frac{a^2}{2}$$

and

$$x = 0 \ ; y = 0 \ \dots \ C_2 = P' \frac{a^3}{6},$$

then

$$EI \frac{dy}{dx} = P \frac{x^2}{2} + P' \frac{(x-a)^2}{2} - P' \frac{a^2}{2}$$

and

$$EIy = P \frac{x^3}{6} + P' \frac{(x-a)^3}{6} - P' \frac{xa^2}{2} + P' \frac{a^3}{6}$$

Then at $x = L$

$$EI \frac{dy}{dx} = P \frac{L^2}{2} + P' \frac{(L-a)^2}{2} - P' \frac{a^2}{2}$$

$$EIy = P \frac{L^3}{6} + P' \frac{(L-a)^3}{6} - P' \frac{La^2}{2} + P' \frac{a^3}{6}$$

The total free end deflection is then given by the deflection caused by the original load P, y_P, and the one induced by the virtual load P', $y_{P'}$,as

$$y_{MAX} = y_P + y_{P'}$$

And the deflection equation is given by:

$$EIy_{MAX} = \frac{PL^3}{6} + \frac{P'}{6}[(L-a)^3 - 3La^2 + a^3]$$

It should be noted that P' is the virtual load causing the increase in the deflection due to the introduced flaw at a distance a, from the free end. Note that if $a = 0$, then $P' = 0$ and the free end deflection and slope reverts back to equation 4.1 and 4.2 respectively:

$$y_{MAX} = \frac{PL^3}{6EI}$$

58

and

$$\frac{d\theta}{dx}_{MAX} = \frac{PL^2}{2EI}$$

Which means this assumption is true from the analysis conducted above and it can be applied to this study as follows:

Figure 4.5 – 4.8 show a linear relationship for each flaw position which proves that the beam sample is still at its elastic form, which brings this study to a finding that showed the trends of the sensor output voltage increasing as the virtual load increases. These results were analysed as shown in the tables on Appendix B.
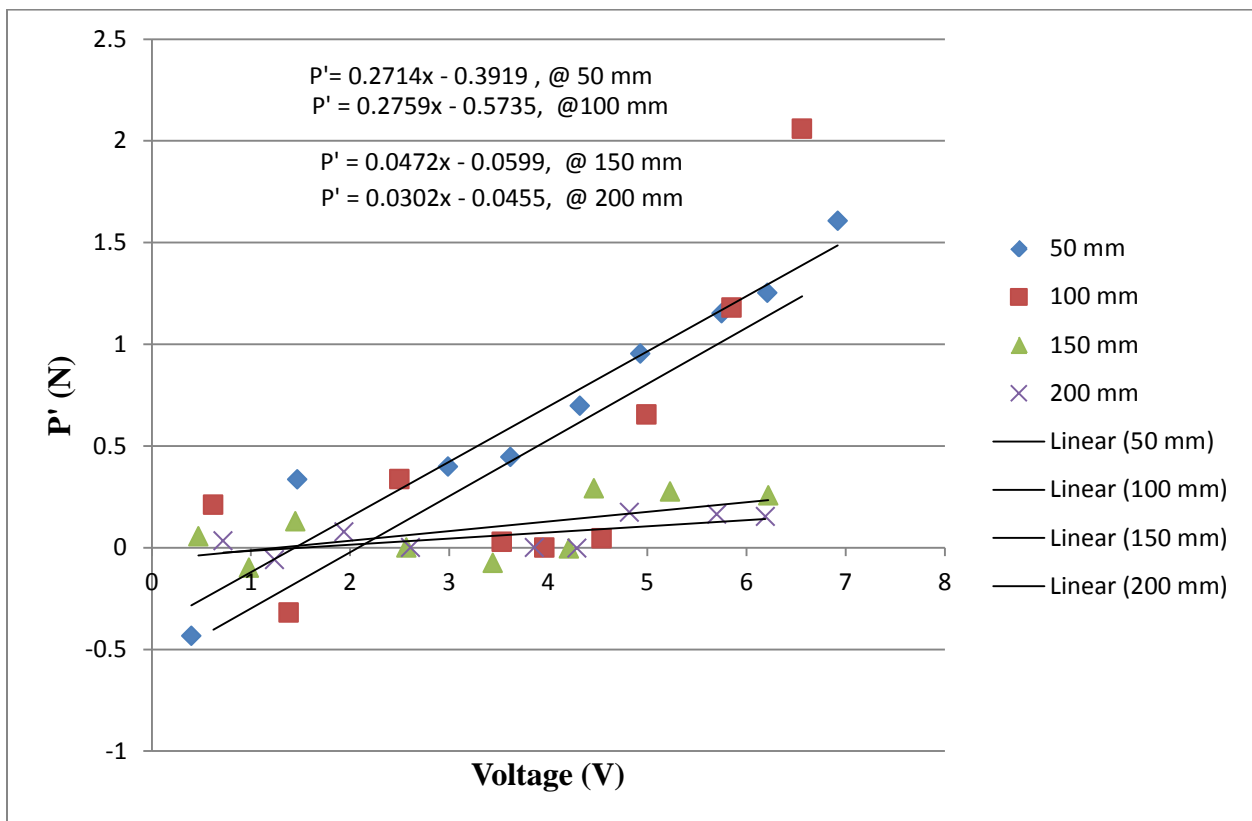
Figure 4.11: Virtual load vs PVDF sensor output

Figure 4.11 still hold for the established fact that when the load increases, the sensor output voltage increases as well but one should keep in mind that the additional load is due to the presence of a flaw in a structure which is the virtual load. It is evident that the virtual load is higher if the flaw is near the fixed end and it decreases as the flaw moves away towards a free end. There were some negative values that resulted on the calculation of the virtual load and that may be due to some errors while taking the readings.

Then,

$$P' = M_1 V + M_2 \qquad\qquad \text{equation 4.3}$$

Where V is the voltage values produced by the sensor, $M_1 \ and \ M_2$ are the slope and P' intercept determined from the graph using the equation of a straight line.

$$EIy_{MAX} = \frac{PL^3}{6} + \frac{M_1 V + M_2}{6}[(L-a)^3 - 3a^2 + a^3] \qquad\qquad \text{equation 4.4}$$

If one wants to determine the location of a flaw, given a voltage reading, the following equation is applicable:

$$a = \frac{1}{3}[L - \frac{6EIy_{MAX}}{L^2(M_1 V + M_2)} + L\frac{P}{M_1 V + M_2}] \qquad\qquad \text{equation 4.5}$$

With this method one is able to determine the geometric location of a particular flaw and a location algorithm has been developed, this finding fulfils objective 1.2.3 of the study.

Chapter five

5. Experimental Vibration tests versus Finite Element Analysis predictions

5.1 Introduction

Carbon fibre has defined material properties as a single layer, but when the two or more layers of carbon fibres are bonded and have a comet layer sandwiched between them to form a composite structure during the infusion process, the material properties change. The material properties for the specimen were determined by means of a three-point bending test and the results were compared with those obtained through the use of Finite Element Analysis, ANSYS Workbench software in this case. The same samples that were used in chapter four were then tested in the following experiment using vibration loading. Experiment and simulation results were then compared.

5.2 Experimental methodology

Figure 5.1 and 5.2 show the apparatus used consisting of the digital vertical Vernier, Fluke-View oscilloscope that was connected to a laptop for data logging, a fixed sample holder and a beam sample equipped with a PVDF sensor attached at the bottom centre line. The sample was 280 mm long and the sample holder clamped the sample at 50 mm. The sensor was placed at the centre of the beam sample which was manufactured in the same way described in chapter 3. The damage position on these samples was the same as the ones used in chapter 4, where a 3 mm through hole was drilled at the centre line at distances of 50 mm, 100 mm, 150 mm and 200 mm from the fixed end respectively. The beam samples were deflected to a maximum deflection value that was measured by a digital vertical Vernier in presence of the mass pieces and it was let

to vibrate freely so as to measure its natural frequency. This method allowed the PDVF sensor to detect those vibrations and give the output as electric signal (Voltage and Frequency).

Figure 5. 1: Experiment set-up and sensor attachment

Figure 5.2: Experiment set-up and loading

5.3 Settings on the Fluke View Oscilloscope

Frequency domain - in frequency domain, the Fast Fourier Transform (FFT) program build in the oscilloscope was used to obtain the resonance response of the sample from the time domain measurements. Typical output of the vibrating sample due to loading is shown in figure 5.3 as well as the settings on the oscilloscope.
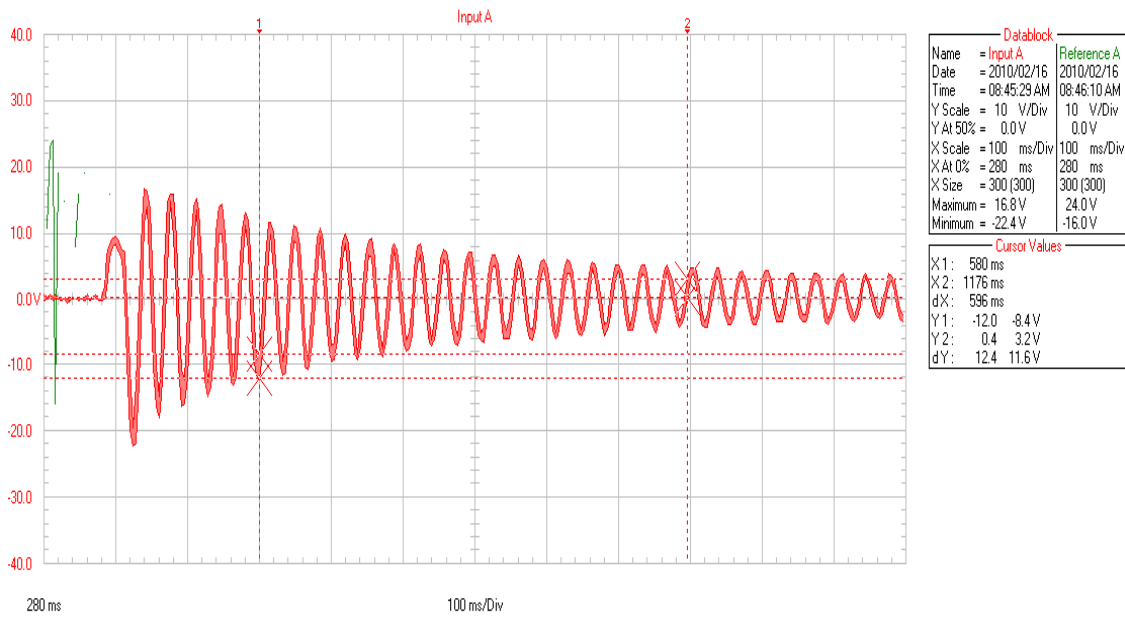
Figure 5.3: Settings on the Oscilloscope

5.4 Natural frequency experimental measurements results

The variation in natural frequency is dependent on the defect's position. As the damage position moves away from the fixed end, the natural frequency increases, approaching the defect free beam's natural frequency. The table with data as provided in sample A to D was prepared and the graph of the natural frequency versus flaw position was plotted using Origin 6.1 software. This experiment produced almost a straight line which enables one to locate a defect anywhere along the length of the sample because it proved that, the closer the flaw to the fixed end, the

higher the natural frequency and the deflection is high as well. This finding partly satisfy objective 1.2.4 because if the flaw is severe then the natural frequency will be high but some more research still need to be done to quantify the severity and conduct damage mechanism to determine the severity of a particular flaw.

In chapter 4, mass pieces were added as point load on a beam sample to produce deflections that were measured. Those deflection values were used to simulate a vibration loading on a beam sample using a digital vertical Vernier scale as shown in figure 5.1 and 5.2. The beam samples were labelled as A, B, C and D because of the flaw position on each which was a 3 mm through hole drilled on it. Beam A was damaged at 50 mm, beam B at 100 mm, beam C at 150 mm and beam D at 200 mm from the fixed end. The beam sample was loaded at known deflections and set to vibrate freely while recording the natural frequency values up to a maximum deflection recorded for a particular flaw position. See appendix C for some random spectrum produced by the PVDF sensor on each test.

Table 11 Experiment results for dynamic loading				
Load (N)	Beam A (Hz)	Beam B (Hz)	Beam C (Hz)	Beam D (Hz)
0.49	25.25	26.57	27.4	29.09
0.98	25.25	26.57	27.4	29.09
1.47	25.25	26.57	27.4	29.09
1.96	25.25	26.57	27.4	29.09
2.45	25.25	26.57	27.4	29.09
2.94	25.25	26.57	27.4	29.09
3.43	25.25	26.57	27.4	29.09
3.92	25.26	26.57	27.4	29.09
4.41	25.26	26.57	27.4	29.09
Average	25.25	26.57	27.40	29.09
Maximum deflection (mm)	12.11	10.81	9.26	8.61
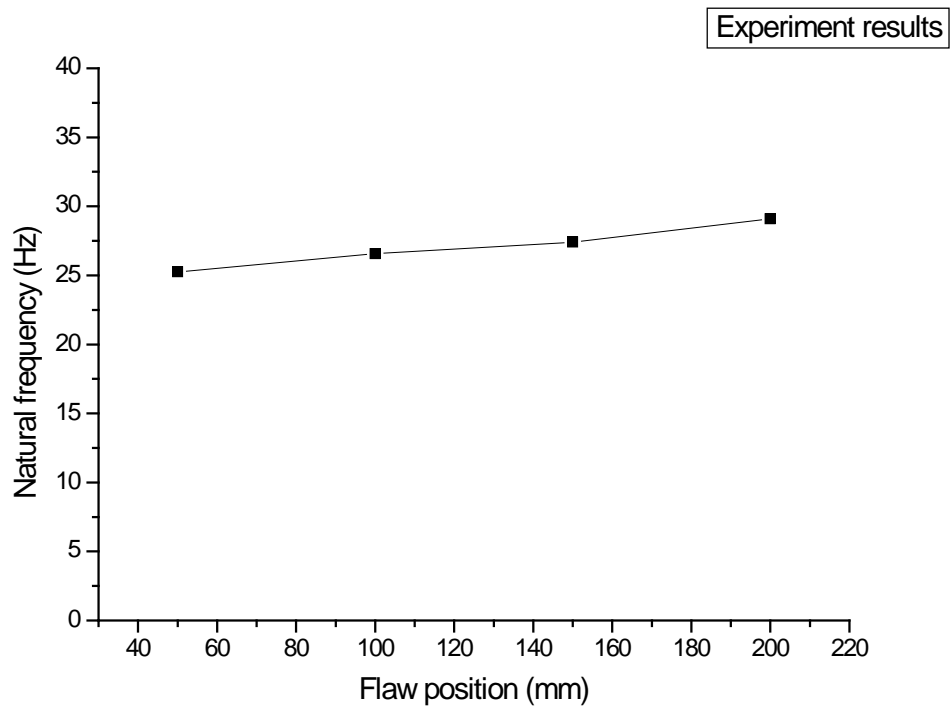
Figure 5.4: Frequency of flawed beam as a function of position (experiment)

5.5 Natural frequency simulation measurement results

The software that was used for Finite Element Analysis (FEA) was ANSYS Workbench V.14.5; it has the capability to interface with other design and simulation software like solid-works. A beam sample design was drawn using Solid-works software, the drawing was saved as Para-solid in Solid-work so that it contains an x*t extension file compatible to ANSYS. The beam sample was imported to ANSYS software for analysis. The specimen was modelled as a beam with damaged segment of reduced elastic modulus due to the presence of the defect of 3 mm through hole at different locations which were the same as beam A, B, C and D using Solid-works. A simulated load was added to the beam sample following the same procedure as described in point 5.4 of this chapter.

65

The following assumptions were made:

- The geometrical configuration of the beam remains unchanged meaning the cross section remains constant.

- The damage was represented by a small change (3 mm through hole) in elastic modulus that affects the stiffness of the beam.

- The beam remains in the elastic region when it was in the damage state.

- The damage occurs within the domain of the system and the boundary conditions for static and dynamic case remain unchanged compared to the undamaged case.

The material properties that were used as the engineering data were as follows: Young's Modulus was 1.86 GPa, maximum flexural stress was 0.123 GPa and polar moment of inertia (I) was $4.6e^{-11}$. See appendix D for the output of ANSYS Transient Structural test graphs.

Table 12 Finite Element Method results for dynamic loading		
Damage position (mm)	Natural frequency (Hz)	Maximum deflection (mm)
50	32.1	12.11
100	34.2	10.81
150	35	9.26
200	35	8.61
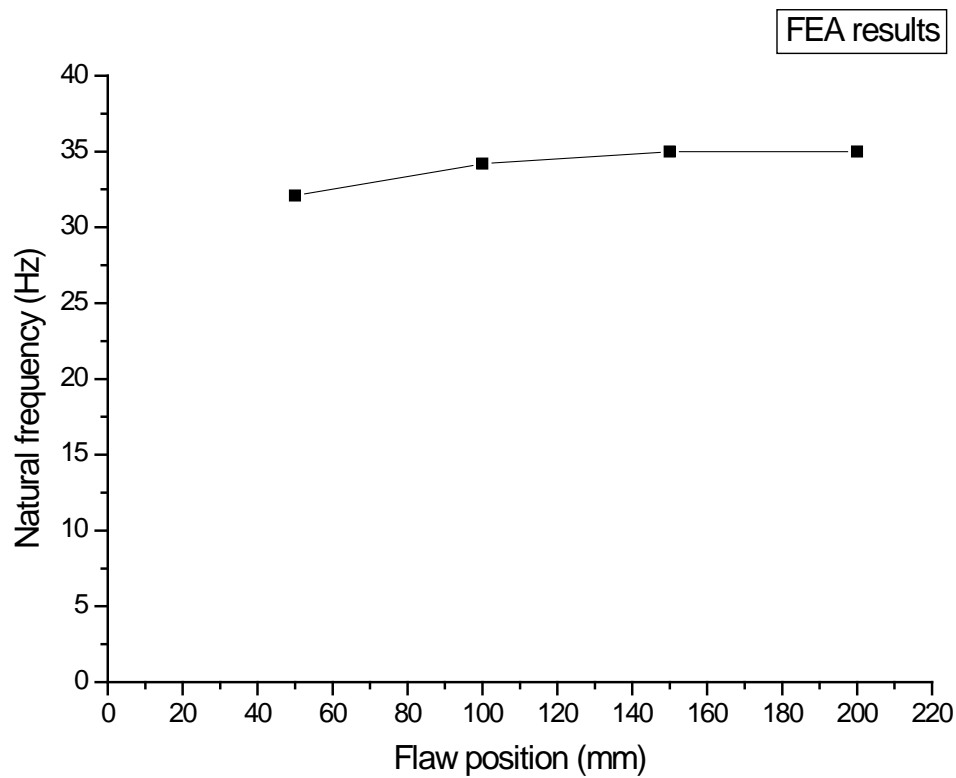
Figure 5.5: Frequency of flawed beam as a function of position (simulation)

Comparison between the experiment results and the simulation results was conducted and both results showed a difference of 25%. The main fact that came out of these results was the fact that both experiment and simulation results have the same trend although there was a difference in the natural frequency values. The following chapter discusses and justify the possible factors that could be the reasons for the difference.

Table 13: Experiment and FEM results compared

FEA results for dynamic loading			Experiment results for dynamic loading	
Damage position (mm)	Natural frequency (Hz)	Maximum deflection (mm)	Damage position (mm)	Natural frequency (Hz)
50	32.1	12.11	50	25.25
100	34.2	10.81	100	26.57
150	35	9.26	150	27.4
200	35	8.61	200	29.09
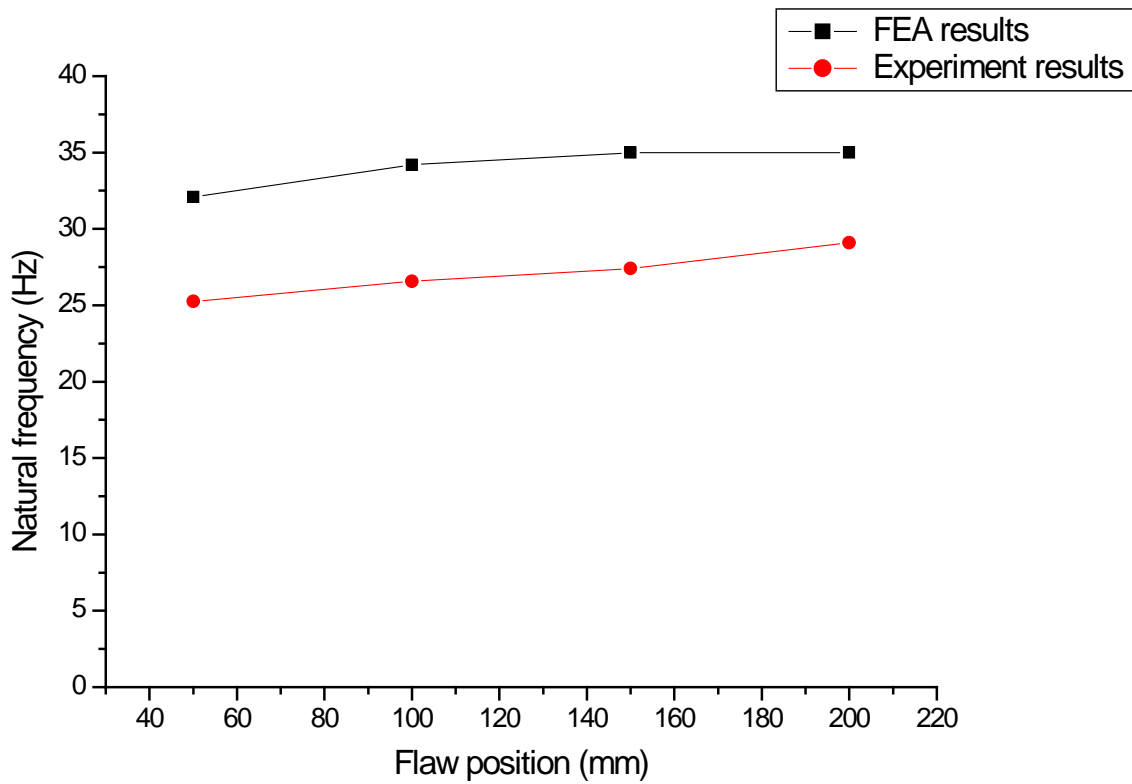
Figure 5.6: Frequency Vs Flawed position - Experiment and FEM results

Chapter six

6.1   Discussion

The Department of Mechanical Engineering of the Cape Peninsula University of Technology has made some advancement as far as SHM technique for aeronautical industry. This is evident on the identification of the presence of a defect on Guardian II, the UAV wing study was conducted using the following techniques, Digital Shearography for defect identification, position and sensor to structure interaction, the embedded PVDF film sensor for impact and vibratory load analysis of the UAV wing and Finite Element Analysis (ANSYS Workbench) which served as a modelling tool to predict the presence of defects in the wing model by investigating the change of natural frequency of first mode of vibration. All the methods used in this study were investigated in detail and the following discussion enables the choosing of PVDF for condition monitoring the UAV wing structure.

6.1.1   Digital Shearography

Digital Shearography is a NDT technique of identifying hidden defects in composites that has been used for years and produces good and reliable results. It has high sensitivity and can measure strains from 20 $\mu\varepsilon$ upwards; however it has some limitations. The idea was to have a system that will continuously interrogate the structure while it is in service so as one can predict the remaining life of the structure as outlined in the objectives on page 2. The UAV wing experiences a much higher vibrational loading during landing. This technique requires the

structure to be in a stationary position during the inspection process. Any disturbance will destroy any possible formation of interference fringes and render the inspection procedure useless. Measurements of strains in complex surfaces are possible with additional data processing but it's not possible to measure or inspect a big surface of the material while in motion so thereby defeating objective 1.2.2. In this case an embedded sensor such as PVDF sensor can be employed to signal the presence of a defect/flaw which will enable Shearography subsequently to quantify the severity of the flaw and fracture mechanics using material properties when the structure is stationary. The Digital Shearography results on chapter 3 clearly showed that the attachment method used to embed the sensor to a structure was not spurious because after the structure was fractured on a three-point bending test there was a voltage spike at different time intervals. This technique meets objective 1.2.3 but it has a limitation that the structure must be stationary as seen on the results on chapter 3.

6.1.2 Finite Element Analysis

ANSYS is one of the leading commercial simulation programs for solving engineering problems in disciplines like dynamic, statistic, heat flow, electromagnetism etc. One needs to understand that the finite element analysis solutions will always be an approximate solution of the problem. The experimental results will correct the simulation results. In this investigation ANSYS Workbench was used taking into account the risk of making modelling mistakes. Active vibration-based method and model-based methods are applied in SHM to undertake structural model analysis and use model characteristic parameters to identify defects; this is the one of the best methods that allows the use of such techniques, as shown in the simulation results in figure 5.5.

6.1.3 Embedded PVDF sensor

The focus of this investigation was to develop a good understanding of the practical and theoretical framework of the PVDF sensor and couple it to the Guardian II wing structure for damage detection. To achieve that one had to identify the type, make-up and material properties of the composite to be used, which was objective 1.2.1. This objective was achieved in chapter 2 where the infusion process was studied in details and specimens of 280 mm X 69 mm X 2 mm were manufactured using carbon fibre laminates where comet was sandwiched between the layers of carbon fibre. Carbon fibres were laid-up in bidirectional orientation at 90^0 because those types of orientation have strength in both directions. The material properties were obtained using a three-point bending test as explained in chapter 3.

A method for determining online damage identification which requires the identification of a particular sensor for the work environment was achieved and is evident in the related literature in chapter 1 where point number 1.4 talks about the different Structural Health Monitoring methods of which the piezoelectric sensor (PVDF) took precedence thereby satisfying objective 1.2.2.

The FEA and experimental results showed satisfactory agreement about the presence of the damage and the position of the damage looking at the trend of the results in a graph in figure 5.6. However there was a difference in the results simulation and the experiment of about 25 % and the difference in these results can be attributed by the following:

- Modelling the PVDF film sensor which was not included in the FEA.
- Estimation of the change of Young's modulus in the volume of the defect in the FEA
- Properties of the bonding layers which were neglected.
- The mass and rigidity of the PVDF sensor that was added to the structure

- The mass of the material removed when introducing the defect was not taken into account.

Objective 1.2.4 was partly attained because looking at the results in figure 5.6, one can conclude by saying, the more severe the flaw, the larger the natural frequency but there still is more work to be done here. So if a structure is reporting large natural frequency values then the UAV must be landed to conduct fracture mechanics and techniques like Digital Shearography can be employed.

6.2   Conclusion

Literature revealed that while the field of structural health monitoring has been researched for some time, there is still a lack for a workable online structural health monitoring technique relating to the real world application. Variability of new age composite materials poses complicated problems relating to SHM and analysis techniques. The focus of this research was to study the feasibility of using polymeric piezoelectric sensor (PVDF) because it is flexible compared to PZT which is brittle.

6.2.1   Research outcomes

The majority of the objectives set for this study were achieved except for objective 1.2.5 which is about the prediction of the remaining life of the structure. The infusion process was studied in details and an experiment using carbon fibre was conducted at Advanced Manufacturing Technology Laboratory (AMTL) at CPUT and the material properties of a composite wing structure were determined. The proposed method based on numerical and experimental data to predict the effect of damaged parameters on a composite UAV wing sample has shown that for

the type of flaws considered in this study and its relative location along the sample length affects the dynamic and static conditions of the structure. This study showed that if the damage was closer to the fixed end, the deflection was high and the sensor output voltage was high, that was due to the fact that near the fixed end it is the area of high stress concentration. It was proved that the presence of the flaw in a structure possess an additional load which can be identified as a virtual load. So using that one can be able to determine a geometric location of a particular flaw using the algorithm developed in chapter 4, that satisfy objective 1.2.3.

For the advancement of the structural health monitoring technique at CPUT, Mechanical engineering department, this study has taken a first step in solving a challenge of damage identification on a Guardian II wing structure. This technique is applicable on UAV usage period, where the tests can be carried out on certain time intervals because in the presence of damage on the wing, the PVDF sensor will record a high value of the voltage and the natural frequency. This is regarded as a virtual load that is added due to the presence of a flaw, and then a UAV must be landed to assess the problem. Equation 4.5 can be used to determine the geometric location of the flaw along the wing structure. This technique is cost serving because there is only one sensor that is strategically placed near the fixed end of the wing instead of using an array of sensors for damage position identification and it also simplifies wiring, data transmission and analysis complexity. The major fact is the reduced down-time during maintenance because using this technique, there is no need to scan the whole UAV but one can focus on the location determined by equation 4.5 and that saves time so that the UAV can be back to service again.

The natural frequency increases as the damage moved away from the fixed end and thereby one can draw a conclusion that, PVDF sensor is a potential sensor for determining the geometric location of a particular flaw. Looking at the trend in the Natural frequency vs Flaw position graph, the results show a linear relationship. One can predict that if the flaw is high then the sensor output will also be high so that one can be able to quantify the severity of the damage which is a first step in addressing objective 1.2.4.

PVDF sensor is a suitable sensor for strain measurements on a UAV wing as it gave real-time values. This sensor makes it possible to monitor a large area of the structure. The PVDF sensor was able to detect all the strains in the structure as it was laminated on the surface, perhaps a disadvantage because it can be damaged due to exposure to environmental situations. If it was sandwiched between the layers that would have made it less effective because it would be sitting on the neutral axis and it self can create a void in the structure. The PVDF sensor material has proven to be strong and durable during the testing. PVDF sensor is not suitable for static measurement, this was confirmed during the test and that is why the measurements with this sensor are limited to dynamic conditions.

Finite element analysis can be used to provide a numerical modelling of the structure. PVDF is one of the efficient sensor technologies of online-SHM because it has many advantages over the others which include high flexibility, low mass and cost and high internal damping. This work is a leading study towards the development of the standard for UAV Structural Health Monitoring. The findings of this research can be the starting point in the advancing of the feasibility of using PVDF sensor for online SHM system.

6.3   Recommendations and future work

It is recommended that more extensive studies should be dedicated to the analysis of the effects of different types of defects on the PVDF sensor efficiency and it should involve defect size, number and spatial distribution to predict the remaining life of the overall structure which was objective 1.2.5 and that was not done in this study. Some other aspects that are also of interest include the geometry of the structure on sensing abilities. However it is worth mentioning that the PVDF sensor is not recommended for static measurements because it relies on its piezoelectric effect to be functional and since this sensor has a pyro-electric effect, which means as the temperature increases also the sensor output increases so caution must be taken in conducting measurements in a variable environmental conditions. Perhaps for every PVDF sensor attached, there must be a dummy PVDF sensor placed at 90^0 as a rosette. An in-depth study of using PVDF sensor is recommended where the sensor will be tested on the full-scale UAV wing and real-life environmental situation perhaps that will lead to the prediction of the remaining life of the composite structure. Fracture mechanics to determine the severity of a particular flaw is recommended as future work for this study.

References

[1] K. Diamanti, C. Soutis (2010), *Structural health monitoring technique for aircraft composite structures.* Department of Mechanical Engineering (Aerospace), The University of Sheffield, Mappin Street, Sheffield S1 3JD, UK.

[2] [a]S. Masmoudi, [a]EI Mahi, [b]S. Turki and [b]E.I. Guerjouma (2012), *Structural Health Monitoring of Smart Composite Material by Acoustic Emission*, [a]Laboratoire d'acoustique de l'université du Maine, B^at. IAM - UFR Sciences Avenue Olivier Messiaen 72085 Le Mans Cedex 9,

[b]Faculté des Science de Sfax, Département physique, B.P. 1171, 3000 Sfax, Tunisia masmoudi.sahir@yahoo.fr.

[3] F.C. Campbell, *Structural composite materials,* Ohio, ASM International, 2010.

[4] Z.K. Awad, T Aravinthan, Y Zhuge, et al, *A review of optimization techniques used in the design of fibre composite structures for civil engineering application,* Materials and Design 2012, 33(1) 534-544.

[5] X.L. Qing, A Kumar, C Zhang, *An active diagnostic system for structural health monitoring of rocket engines,* Journal of intelligent material systems and structures, 20006, 17(7) 619-628.

[6] J. Cai, L. Qui, S. Yuan, L. Shi, P. Lui, D. Liang, *Structural health monitoring for composite materials*, Intech, 2012.

[7] M. Baskar Rao, M.R. Bhat, C.R.L Murthy, K. Ven Madhav, S. Asokan, *Structural health monitoring (SHM) using strain gauges, PVDF film and fibre bragg grating (FBG) sensors: A comparative study,* Proc. National Seminar on Non-Destructive Evaluation, Dec. 7 – 9, 2006, Hyderabad.

[8] T. Kleckers, *Electrical strain gauge, piezoelectric sensors of fibre bragg sensors for force measurement: Prospect and potential,* Hottinger Baldwin Messtechnik GmbH, Darmstadt Germany.

[9] Kyowa Electronic Instruments Co. LTD, 3-5-1, *www.kyowa-ei.com,* Chofugaoka Chofu, Tokyo 182-8520, Japan. Accessed 22 May 2013.

[10] H.N. Lia, D.S. Lia, G.B Song, *Recent applications of fibre optic sensors to health monitoring in civil engineering structures*, 2004, 26(11): 1647-1657.

[11] R. Di Sante, *Fibre Optic Sensors for Structural Health Monitoring of aircraft composite structures: Recent advances and applications*, 30 July 2015, Department of Industrial Engineering – DIN, University of Bologna, Forli 47121, Italy.

[12] S. Thakral, P. Manhans, *Fibre optic sensor technology & their applications*, June 2011, Dept. of ECE, Manav Rachna International University (MRIU) Faridabad, Haryana, India.

[13] H.A. Sodano, *Development of anAutomated Eddy Current Structural Health Monitoring technique with extended sensing region for corrosion detection*, Structural Health Monitoring 2007, 6(2): 111 – 119.

[14] I. Raicu, *MEMS technology overview and limitations*, September 2004, Class: CSC8800.

[15] M.L. Roukes, *Nanoelectromechanical Systems*, Tech.Digest.Solid State Sensor and Actuator Workshop, Hilton Head Island, SC 2000.

[16] Measurement specialist. *Piezo Film sensor technical manual (2006).* Available online at, www.meas-spec.com, accessed 11/12/2012.

[17] Yao Fu, Prof. E Harvey, Dr. M Ghantasala and Dr G Spinks, *Design, modelling and fabrication of piezoelectric actuators*, University of Wollongong.

[18] R. Vodicka and Dr. S Galea, 1998. *Use of PVDF strain sensors for health monitoring of bonded composites*. Published by DSTO Aeronautical and Maritime Research Laboratory. Online: www.ndt.defence.gov.au [06/1998].

[19] 2007 Ben Franklin Structural Health Monitoring workshop, *Recent research on damage detection methods for helicopter rotor system,* Penn State, April 12-13 2007.

[20] Giurgiutiu V and Rogers C A, 1998, *Recent advancements in the electro-mechanical (E/M) impedance method for structural health monitoring and NDE*, The SPIE's 5th Annual International Symposium on Smart Structures and Materials, Catamaran Resort Hotel, CA (Paper 29-53).

[21] Gurit Guide to Infusion Part 1, *Technical service report*

[22] Krishna Kr. Hansdah, *3-Point bending test (Flexural test)*, 7 November 2012.

[23] UCT-NDT Digital Shearography DS-03, *Digital Shearography NDT system*, 2008.

[24] Y.Y Hung. *Application of digital shearography for testing of composite structures*, Department of Mechanical Engineering, Oakland University, Rochester, MI 48309, Composite: Part B 30 (1999) 765-773.

APPENDIX A: PVDF sensor properties [16]

Symbol	Parameter		PVDF	Copolymer	Units
t	Thickness		9, 28, 52, 110	<1 to 1200	μm (micron, 10^{-6})
d_{31}	Piezo Strain Constant		23	11	10^{-12} $\dfrac{m/m}{V/m}$ or $\dfrac{C/m^2}{N/m^2}$
d_{33}			-33	-38	
g_{31}	Piezo Stress constant		216	162	10^{-3} $\dfrac{V/m}{N/m^2}$ or $\dfrac{m/m}{C/m^2}$
g_{33}			-330	-542	
k_{31}	Electromechanical Coupling Factor		12%	20%	
k_t			14%	25-29%	
C	Capacitance		380 for 28μm	68 for 100μm	pF/cm² @ 1KHz
Y	Young's Modulus		2-4	3-5	10^9 N/m²
V_0	Speed of Sound	stretch:	1.5	2.3	10^3 m/s
		thickness:	2.2	2.4	
p	Pyroelectric Coefficient		30	40	10^{-6} C/m² °K
ε	Permittivity		106-113	65-75	10^{-12} F/m
$\varepsilon/\varepsilon_0$	Relative Permittivity		12-13	7-8	
ρ_m	Mass Density		1.78	1.82	10^3kg/m
ρ_e	Volume Resistivity		>10^{13}	>10^{14}	Ohm meters
$R_\square$	Surface Metallization Resistivity		<3.0	<3.0	Ohms/square for NiAl
$R_\square$			0.1	0.1	Ohms/square for Ag Ink
tan δ_e	Loss Tangent		0.02	0.015	@ 1KHz
	Yield Strength		45-55	20-30	10^6 N/m² (stretch axis)
	Temperature Range		-40 to 80...100	-40 to 115...145	°C
	Water Absorption		<0.02	<0.02	% H₂O
	Maximum Operating Voltage		750 (30)	750 (30)	V/mil(V/μm), DC, @ 25°C
	Breakdown Voltage		2000 (80)	2000 (80)	V/mil(V/μm), DC, @ 25°C

APPENDIX B: Virtual load and maximum displacement calculations

This study proved that the presence of a flaw in a structure introduces a virtual load, using the following equation; a virtual load can be calculated:

$$EIy_{max} = \frac{PL^3}{6} + \frac{P'}{6}[(L-a)^3 - 3La^2 + a^3]$$

When rearranging the above equation and making P' the subject of the formula, the following equation is produced:

$$P' = (EIy_{max} - P\frac{L^3}{6})\frac{6}{(L-a)^3 - 3La^2 + a^3}$$

Therefore all the parameters involved in the above equation were put on an Excel spreadsheet for analysis as shown below. This was done at known values of *a.* A PVDF sensor output voltage (V) has a linear relationship with a flaw position and there for related to the virtual load, the following straight line equation shows that relationship:

$$P' = M_1V + M_2$$

This work is a first step in developing a standard for condition monitoring of a UAV wing so for a standard set of manufactured wings, such a test must be conducted and these values will serve as reference. For maintenance procedures, the wing will go through these test discussed in this study and if there are adverse values of the sensor output then that mean the wing has some flaws in it. Equation 4.5 is then applicable to determine the flaw position. Also if the sensor gives adverse values during a service of a UAV then that calls for a UAV to be landed for further investigation.

						Virtual load calculation for a flaw position between 0 and 50 mm								
a	L	EI	P	L^3	Y(P)	Y(P&P')	Y(P')	(L-a)^3	3a^2L	a^3	P'	V_0Flaw	V_50Flaw	Delta Flaw
0.05	0.23	7.65E-04	0.49	0.012167	-6.50E-01	-1.05E+00	-4.00E-01	0.005832	0.001725	0.000125	-0.4337	0.3	0.4	0.1
0.05	0.23	7.65E-04	0.98	0.012167	-1.36E+00	-2.09E+00	-7.30E-01	0.000125	0.0135	0.003375	0.33496	0.74	1.47	0.73
0.05	0.23	7.65E-04	1.47	0.012167	-2.23E+00	-3.10E+00	-8.70E-01	0.000125	0.0135	0.003375	0.3992	1.28	2.99	1.71
0.05	0.23	7.65E-04	1.96	0.012167	-3.54E+00	-4.51E+00	-9.70E-01	0.000125	0.0135	0.003375	0.44509	2.25	3.62	1.37
0.05	0.23	7.65E-04	2.45	0.012167	-4.97E+00	-6.49E+00	-1.52E+00	0.000125	0.0135	0.003375	0.69746	3.3	4.32	1.02
0.05	0.23	7.65E-04	2.94	0.012167	-6.07E+00	-8.15E+00	-2.08E+00	0.000125	0.0135	0.003375	0.95442	3.77	4.93	1.16
0.05	0.23	7.65E-04	3.43	0.012167	-7.04E+00	-9.55E+00	-2.51E+00	0.000125	0.0135	0.003375	1.15172	4.67	5.75	1.08
0.05	0.23	7.65E-04	3.92	0.012167	-7.87E+00	-1.06E+01	-2.73E+00	0.000125	0.0135	0.003375	1.25267	5.45	6.21	0.76
0.05	0.23	7.65E-04	4.41	0.012167	-8.61E+00	-1.21E+01	-3.50E+00	0.000125	0.0135	0.003375	1.60599	5.91	6.92	1.01

						Virtual load calculation for a flaw position between 0 and 100 mm								
a	L	EI	P	L^3	Y(P)	Y(P&P')	Y(P')	(L-a)^3	3a^2L	a^3	P'	V_0Flaw	V_100Flaw	Delta Flaw
0.1	0.23	7.65E-04	0.49	0.012167	-6.50E-01	-8.20E-01	-1.70E-01	0.002197	0.0069	0.001	0.21065	0.3	0.62	0.32
0.1	0.23	7.65E-04	0.98	0.012167	-1.36E+00	-1.02E+00	3.40E-01	0.001	0.0069	0.001	-0.3184	0.74	1.38	0.64
0.1	0.23	7.65E-04	1.47	0.012167	-2.23E+00	-2.59E+00	-3.60E-01	0.001	0.0069	0.001	0.33712	1.28	2.5	1.22
0.1	0.23	7.65E-04	1.96	0.012167	-3.54E+00	-3.57E+00	-3.00E-02	0.001	0.0069	0.001	0.02809	2.25	3.53	1.28
0.1	0.23	7.65E-04	2.45	0.012167	-4.97E+00	-4.97E+00	0.00E+00	0.001	0.0069	0.001	0	3.3	3.96	0.66
0.1	0.23	7.65E-04	2.94	0.012167	-6.07E+00	-6.12E+00	-5.00E-02	0.001	0.0069	0.001	0.04682	3.77	4.54	0.77
0.1	0.23	7.65E-04	3.43	0.012167	-7.04E+00	-7.74E+00	-7.00E-01	0.001	0.0069	0.001	0.65551	4.67	4.99	0.32
0.1	0.23	7.65E-04	3.92	0.012167	-7.87E+00	-9.13E+00	-1.26E+00	0.001	0.0069	0.001	1.17991	5.45	5.85	0.4
0.1	0.23	7.65E-04	4.41	0.012167	-8.61E+00	-1.08E+01	-2.20E+00	0.001	0.0069	0.001	2.06016	5.91	6.56	0.65

						Virtual load calculation for a flaw position between 0 and 150 mm								
a	L	EI	P	L^3	Y(P)	Y(P&P')	Y(P')	(L-a)^3	3a^2L	a^3	P'	V_0Flaw	V_150Flaw	Delta Flaw
0.15	0.23	7.65E-04	0.49	0.012167	-6.50E-01	-7.90E-01	-1.40E-01	0.000512	0.015525	0.003375	0.0552	0.3	0.47	0.17
0.15	0.23	7.65E-04	0.98	0.012167	-1.36E+00	-1.11E+00	2.50E-01	0.000512	0.015525	0.003375	-0.0986	0.74	0.98	0.24
0.15	0.23	7.65E-04	1.47	0.012167	-2.23E+00	-2.56E+00	-3.30E-01	0.000512	0.015525	0.003375	0.13011	1.28	1.45	0.17
0.15	0.23	7.65E-04	1.96	0.012167	-3.54E+00	-3.54E+00	0.00E+00	0.000512	0.015525	0.003375	0	2.25	2.57	0.32
0.15	0.23	7.65E-04	2.45	0.012167	-4.97E+00	-4.78E+00	1.90E-01	0.000512	0.015525	0.003375	-0.0749	3.3	3.44	0.14
0.15	0.23	7.65E-04	2.94	0.012167	-6.07E+00	-6.06E+00	1.00E-02	0.000512	0.015525	0.003375	-0.0039	3.77	4.21	0.44
0.15	0.23	7.65E-04	3.43	0.012167	-7.04E+00	-7.78E+00	-7.40E-01	0.000512	0.015525	0.003375	0.29176	4.67	4.46	-0.21
0.15	0.23	7.65E-04	3.92	0.012167	-7.87E+00	-8.57E+00	-7.00E-01	0.000512	0.015525	0.003375	0.27599	5.45	5.23	-0.22
0.15	0.23	7.65E-04	4.41	0.012167	-8.61E+00	-9.26E+00	-6.50E-01	0.000512	0.015525	0.003375	0.25628	5.91	6.22	0.31

						Virtual load calculation for a flaw position between 0 and 200 mm								
a	L	EI	P	L^3	Y(P)	Y(P&P')	Y(P')	(L-a)^3	3a^2L	a^3	P'	V_0Flaw	V_200Flaw	Delta Flaw
0.2	0.23	7.65E-04	0.49	0.012167	-6.50E-01	-7.90E-01	-1.40E-01	0.000027	0.0276	0.008	0.03282	0.3	0.72	0.42
0.2	0.23	7.65E-04	0.98	0.012167	-1.36E+00	-1.11E+00	2.50E-01	0.000027	0.0276	0.008	-0.0586	0.74	1.24	0.5
0.2	0.23	7.65E-04	1.47	0.012167	-2.23E+00	-2.56E+00	-3.30E-01	0.000027	0.0276	0.008	0.07736	1.28	1.94	0.66
0.2	0.23	7.65E-04	1.96	0.012167	-3.54E+00	-3.54E+00	0.00E+00	0.000027	0.0276	0.008	0	2.25	2.61	0.36
0.2	0.23	7.65E-04	2.45	0.012167	-4.97E+00	-4.97E+00	0.00E+00	0.000027	0.0276	0.008	0	3.3	3.86	0.56
0.2	0.23	7.65E-04	2.94	0.012167	-6.07E+00	-6.06E+00	1.00E-02	0.000027	0.0276	0.008	-0.0023	3.77	4.29	0.52
0.2	0.23	7.65E-04	3.43	0.012167	-7.04E+00	-7.78E+00	-7.40E-01	0.000027	0.0276	0.008	0.17348	4.67	4.82	0.15
0.2	0.23	7.65E-04	3.92	0.012167	-7.87E+00	-8.57E+00	-7.00E-01	0.000027	0.0276	0.008	0.1641	5.45	5.7	0.25
0.2	0.23	7.65E-04	4.41	0.012167	-8.61E+00	-9.26E+00	-6.50E-01	0.000027	0.0276	0.008	0.15238	5.91	6.19	0.28

Maximum displacement calculations					
	Ymax	Ymax	Ymax	Ymax	Ymax
Load (N)	F_0 (mm)	F_50 (mm)	F_100 (mm)	F_150 (mm)	F_200 (mm)
0	0	0	0	0	0
0.49	0.65	1.05	0.82	0.65	0.79
0.98	1.36	2.09	1.02	1.66	1.11
1.47	2.23	3.1	2.59	2.7	2.56
1.96	3.54	4.51	3.57	3.73	3.54
2.45	4.97	6.49	4.97	4.98	4.78
2.94	6.07	8.15	6.12	6	6.06
3.43	7.04	9.55	7.74	7.11	7.78
3.92	7.87	10.6	9.13	7.84	8.57
4.41	8.61	12.11	10.81	8.61	9.26

APPENDIX C: **Experimental measurement of the natural frequency under dynamic loading.**

The following figures were the results obtained using a FlukeView Oscilloscope Version 4.4, with this oscilloscope one can capture the data and save it or use data logging to save it on the computer. The results were logged in the computer and the following are the replay of some of the screen display of the oscilloscope for different vibratory tests. For each test of the four samples, the process was repeated several times until satisfaction of the repeated results. The vertical Vernier scale ruler was used measure the deflections as the mass pieces were added and the beam deflected. Those deflections were recorded and the beam was let to vibrate freely at those known deflections and the average values from the sensor were recorded for each sample. The following diagrams were some of the replays that were picked randomly from each set of results.
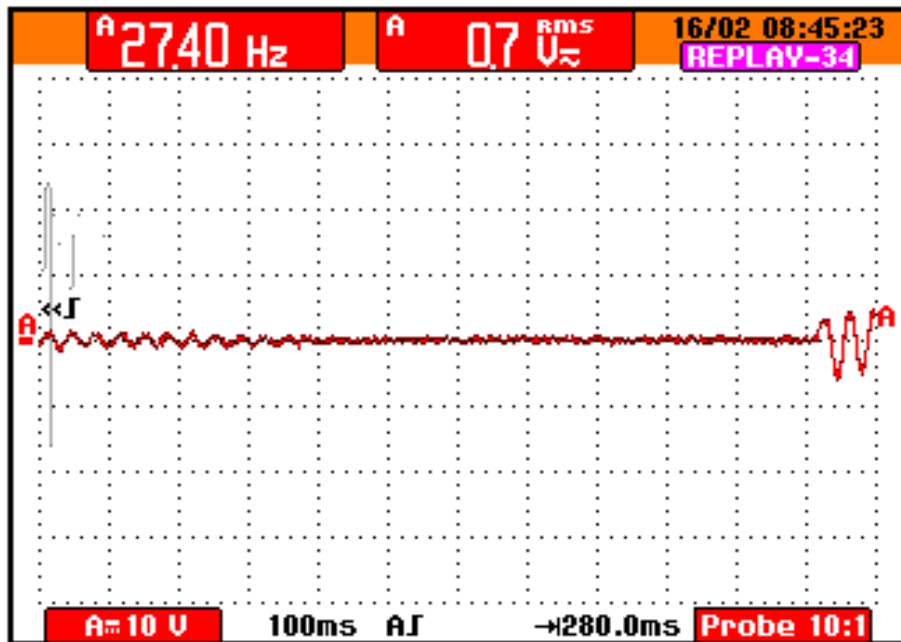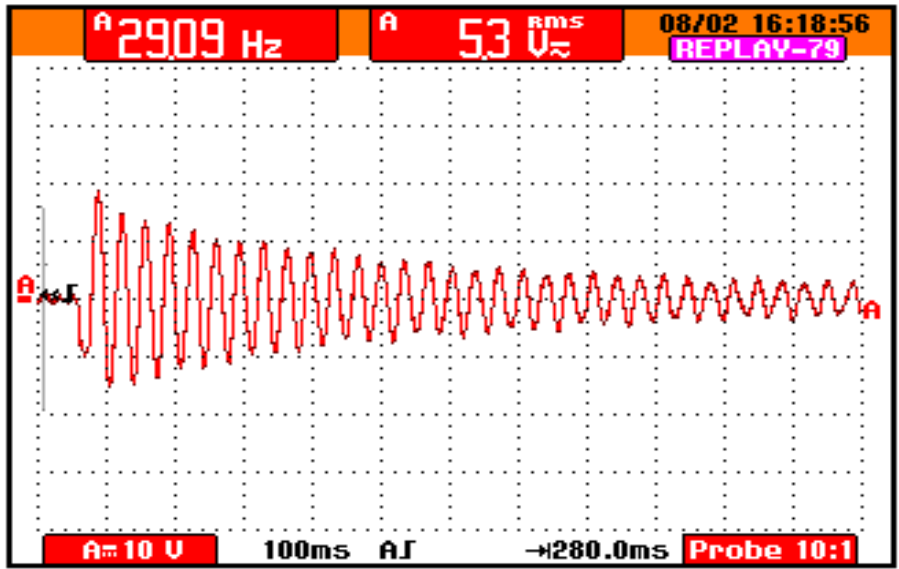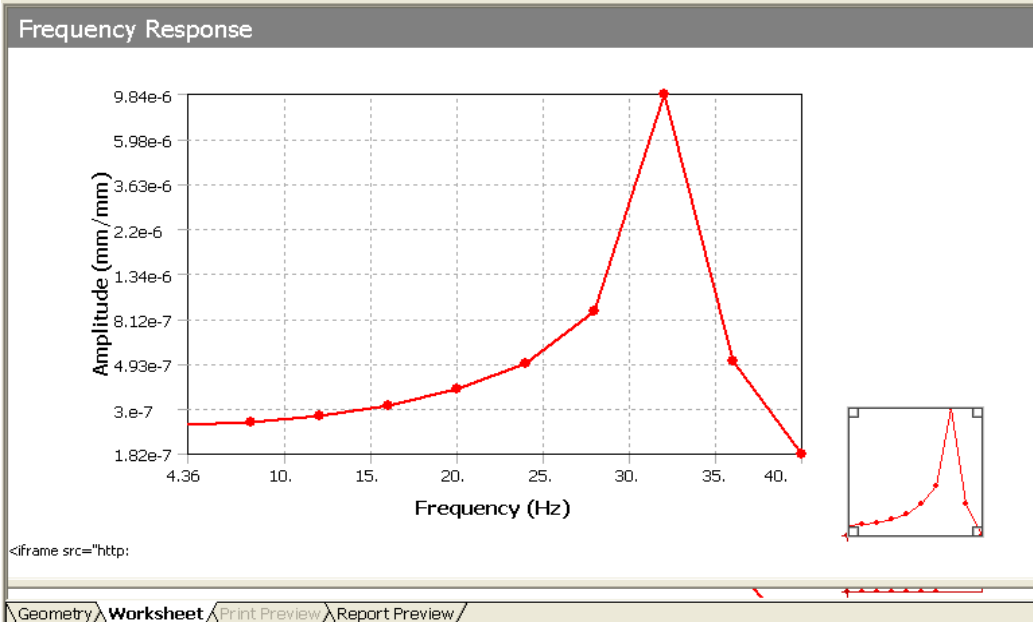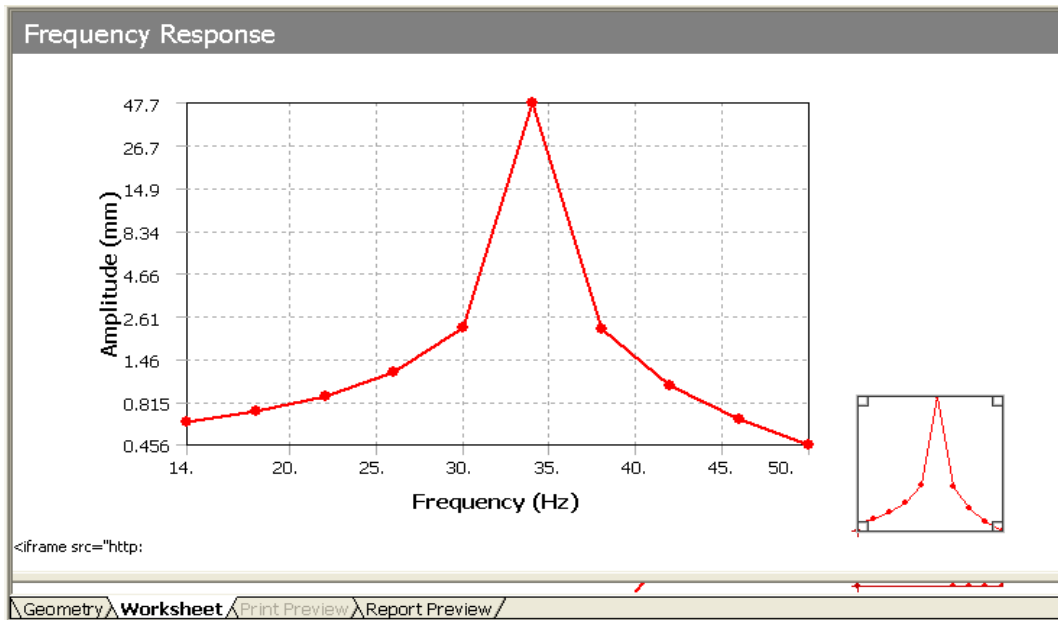

Sample A

Sample B

Sample C

84

Sample D

APPENDIX D: **Finite element method's natural frequency response results.**

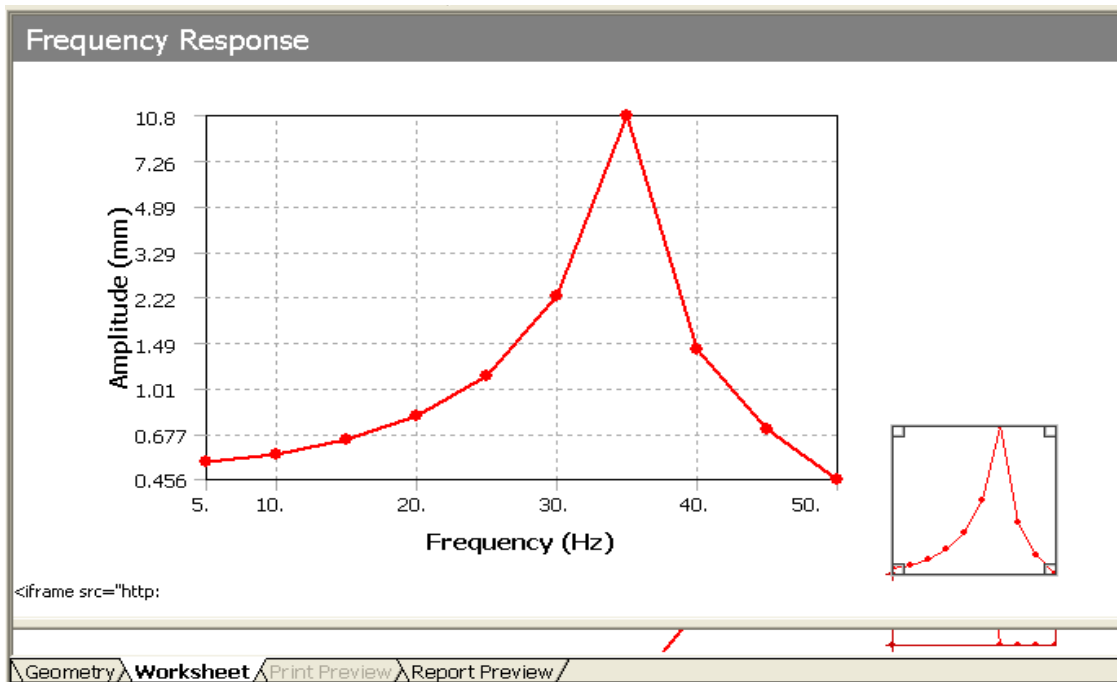The following diagrams are some of the print screen display when the beam was under dynamic
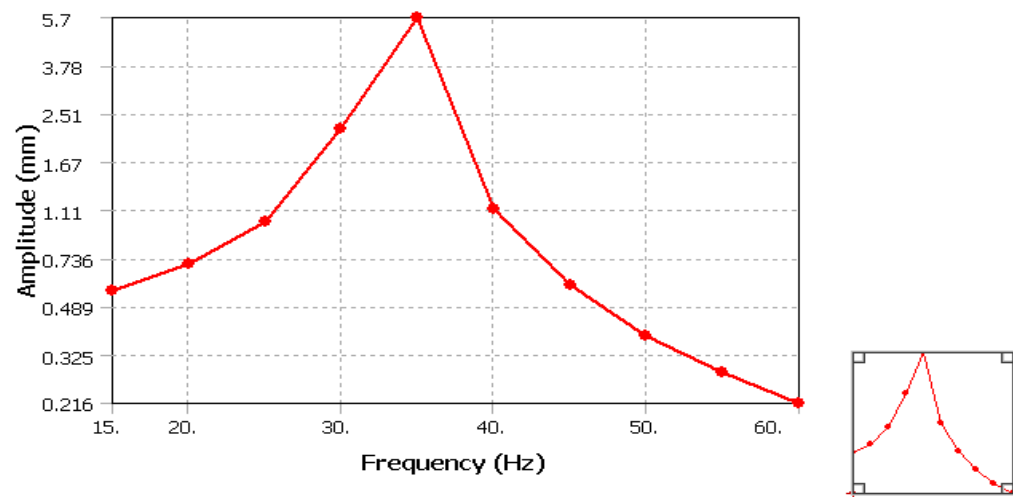
loading using ANSYS Workbench.

Sample A

Sample B

Sample C

Sample D